



Universiteit Utrecht

Master of Sciences Thesis

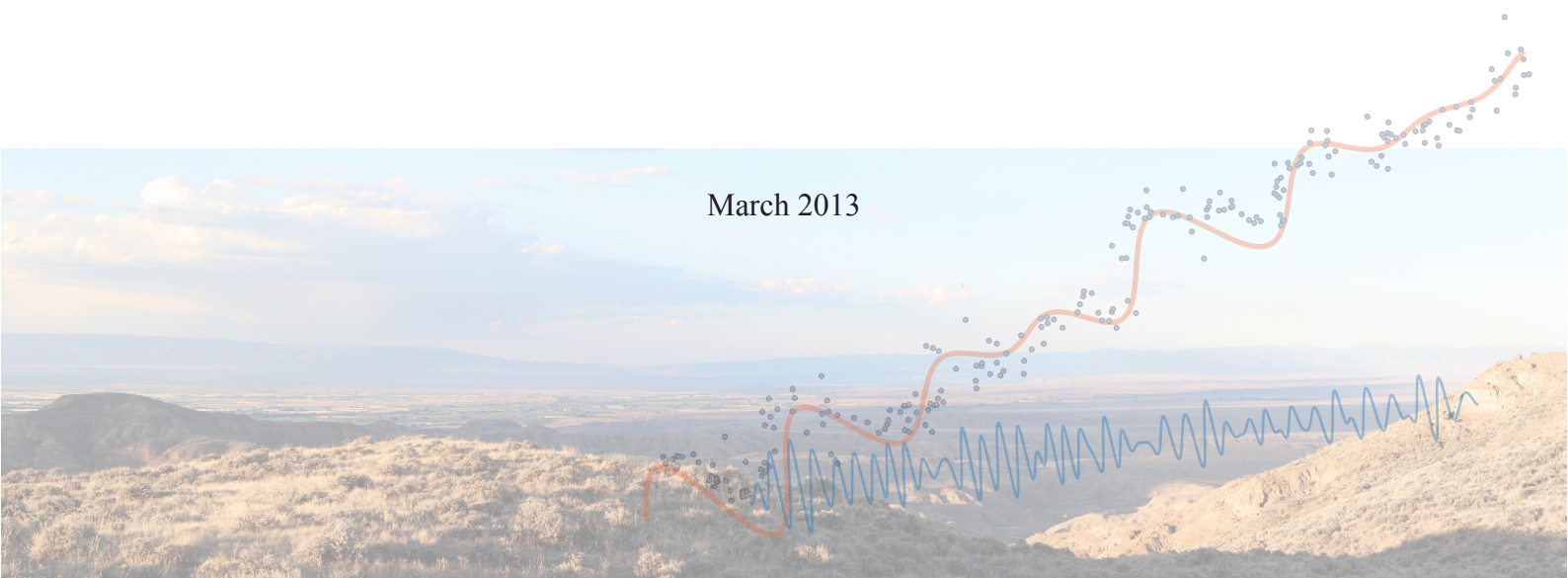
New constraints on Early Eocene hyperthermals; Terrestrial I1 and I2 hyperthermals solve the relation between marine and continental carbon isotope excursion magnitudes.

Utrecht University, Faculty of Geosciences, Department of Earth Sciences

Tarek Marijn Hopman

Supervisors: Dr. H.A. Abels and Dr. F.J. Hilgen

March 2013



“The result, therefore, of our present enquiry is, that we find no vestige of a beginning,—no prospect of an end.”

James Hutton.
Theory of the Earth, 1788.

Table of contents

Abstract	6
1. Introduction	6
2. Geological setting, background and sections	7
2.1. Geological setting	7
2.1.2. Sediments of the Willwood formation	7
2.1.3. Magnetostratigraphy of the Bighorn Basin	8
2.2. Sections	9
3. Methods	9
3.1. Sedimentological description	9
3.2. Carbon isotope data	9
3.3. Principal component analysis and spectral analysis	9
3.4. Paleomagnetism	9
4. Results	9
4.1 Sedimentology	9
4.1.1 Heterolithic deposits	9
4.1.2 Interpretation of the heterolithic deposits	12
4.1.3 Mudrock deposits	12
4.1.4 Interpretation of the mudrock deposits	12
4.2 Pedogenic maturity	12
4.2.1 Cyclicity in the paleosol maturity	12
4.2.2. Interpretation of the lithological alternations	12
4.3. Color data, principal component analysis and time series analysis	13
4.3.1. Principal component analysis (PCA)	13
4.3.2. Time series analysis of the color data	14
4.3.3. Bandpass filtering of the color records	14
4.4. Paleomagnetism	14
4.4.1. Polarity pattern	18
4.5. Carbon nodule isotope data	19
4.5.1. The isotope record of the WB section	20
4.5.2. The isotope record of the DCA section	20
4.5.3. Composite carbon isotope record - "Deer Creek composite"	20
4.6. Cyclostratigraphic integration	20
5. Discussion	23
5.1 Orbital forcing in the WB section	23
5.1.1. Precessional forcing	23
5.1.2. Eccentricity orbital forcing	23
5.1.3. I1 and I2 hyperthermals in the WB section	24
5.2. Comparison of the WB section and hyperthermal magnitudes to the marine realm	24
5.2.1. Comparison of the WB section to the marine realm	24
5.2.2. Magnitudes differences between marine en continental hyperthermals	24
5.2.3. Origin of the depleted $\delta^{13}\text{C}$	26
5.3. Magnetostratigraphic correlation to the Geological Time Scale 2012	27
5.3.1. The C24r/C24r reversal boundary in the Bighorn Basin	27
5.3.2. Comparison to the marine magnetostratigraphic records	27
5.3.3. Dating the C24r/C24n reversal	28
6. Conclusions	29
7. Acknowledgements	29
8. References	30-31

Table of figures

Figure 1: Location of the sections	8
Figure 2: Field log of WB section	10-11
Figure 3: Avulsion/overbank cycles in the field	13
Figure 4: PCA component analysis	13
Figure 5: Color data against lithology	15
Figure 6: Spectral analysis for the color records	16
Figure 7: Zijderveld diagrams for indicative paleomagnetic samples	16
Figure 8: Equal area plots	17
Figure 9: Paleomagnetic results for the WB section	18
Figure 10: $\delta^{13}\text{C}$ and $\delta^{18}\text{O}$ records for the WB section	19
Figure 11: Deer Creek Composite carbon isotope record	21
Figure 12: Deer Creek Composite power spectra	21
Figure 13: Summary of the color and carbon isotope data for the WB section	22
Figure 14: Comparison of the WB section to the marine record	25
Figure 15: CIE comparison of continental and marine hyperthermals	26

Table of appendices

Appendix 1: Paleomagnetic interpretations for the ChRM directions	32
Appendix 2: Isotope data WB section	33
Appendix 3: Isotope data DCA section	36

Abstract

During the Early Eocene (~56-46 Ma), the Earth's climate underwent a series of events that led to relative rapid global warming. The events, or hyperthermals, comprehended a relative fast temperature rise linked to extreme greenhouse conditions. Those greenhouse conditions were fueled by carbon injection to the atmosphere, but the origin of the carbon is still unclear. The occurrence of the hyperthermals is in pace with eccentricity related orbital forcing. Continental hyperthermal carbon isotope excursions magnitudes from paleosol carbonate are found to be consistently higher than their marine equivalents. The relation of how carbon isotope excursion magnitudes are recorded during hyperthermals between the continental and marine records is not resolved. Solving this relation would be an important step towards the understanding of the origin of the injected carbon. Until now, a lack of documented continental hyperthermals hamper the understanding of this relation. We present a carbonate isotope record from paleosol carbonate nodules from the Bighorn Basin, Wyoming. Our section shows, for the first time, the I1 and I2 hyperthermals with $\delta^{13}\text{C}$ magnitude excursions of respectively -2.7‰ and -1.8‰. Further, we constrain a cyclostratigraphic framework containing short and long eccentricity, and precession signals. With this framework we relate our section to the marine realm and show that the cyclostratigraphic framework for both realms are similar. Paleomagnetic study shows a major polarity change, the C24n/C24r reversal boundary, to be present in the short eccentricity maximum after hyperthermal H2. Scaling of five marine and continental hyperthermals inhibits an exponential relation, implying that the same process or processes underlie all of the hyperthermals. Therefore, we exclude hypotheses that do not fit this requirement and causes that do not include orbital forcing.

1. Introduction

Understanding hyperthermals could play a key role as an analogue for the greenhouse climate state as we see nowadays, and therefore these events are extensively studied. However, even though an extensive amount of research has been published on this topic, the hyperthermals are still not fully understood.

The most pronounced hyperthermal is the Eocene Thermal Maximum (PETM) that marks the Paleocene/Eocene boundary (~56 Ma). The PETM is characterized by an increase in surface and deep water temperatures of 4-7°C, a mass extinction of benthic foraminifera, ocean acidification (Kennett and Stott, 1991; Zachos et al., 2005) and shifts in flora and fauna (Zachos et al., 1993; Thomas and Shackleton, 1996; Bowen et al., 2001, 2004).

The extreme and transient hyperthermals have been documented in bulk carbonate, organic matter and foraminiferal carbonate isotope records as negative excursions. The first marine record of the PETM was published by Kennett and Stott (1991) and shows a negative carbon isotope excursion (CIE) of 2-4‰. Nowadays marine records of the PETM are numerous (McInerney and Wing, 2011 and references therein) and marine records showing the presence of other hyperthermals have been presented by several authors (Cramer et al., 2003; Lourens et al., 2005; Stap et al., 2009; Sexton et al., 2011). Early Eocene hyperthermals following the PETM have been labeled by Cramer et al. (2003). The first four in stratigraphic order after the PETM are known as H1 (also known as ETM-2), H2, I1 and I2. Hyperthermals H1 and H2 from the marine realm are described by Stap et al. (2010) with CIE magnitudes of -1.4‰ and -0.8‰ from benthic foraminifera, and comprise a deep ocean warming of respectively ~3°C and ~2°C.

Massive releases of carbon during hyperthermals are needed to explain the extensive dissolution of deep-ocean carbonates, the CIE spike and the relative short durations. The duration of the PETM including recovery tail from cycle counting is estimated to be ~157 kyr (Abdul Aziz et al., 2008) or 120-220

kyr from He³ measurements (Murphy et al., 2010).

Since organisms create $\delta^{13}\text{C}$ depleted carbon by fractionation of carbon during biosynthesis, the carbon was most likely organic carbon (McInerney and Wing, 2011). Possible sources for the depleted carbon are gas hydrates (methane) from the seafloor (Dickens and O'Neil, 1995; Dickens, 2011; Lunt et al., 2011), a meteorite impact (Kent et al., 2003), redistribution of oceanic carbonate (Sexton et al., 2011), magma injection in carbon rich sediments (Svensen et al., 2004), exposure of marine sediments by drying of epicontinental seas (Higgins and Schrag, 2006), thawing permafrost (DeConto et al., 2012) or peat burning (Kurtz et al., 2003).

The drawdown of the carbon that let $\delta^{13}\text{C}$ values to return to pre-hyperthermal situations depends on the origin of the carbon, but is most probably controlled by the sequestering of depleted carbon by the burial of organic matter as soils and peat (Bowen and Zachos, 2010).

The total amount of carbon added to the atmosphere and the $\delta^{13}\text{C}$ fingerprint of the injected carbon control the $\delta^{13}\text{C}$ value of the atmosphere during hyperthermals (McInerney and Wing, 2011). The latter cannot be derived directly from paleorecords since all carbon sinks differentiate from atmospheric values during carbon uptake (Sluijs and Dickens, 2012). When taking PETM CIE values of -2.5 to -4.0‰, the PETM can be explained by the release of ~2000-3500 Gt carbon with a $\delta^{13}\text{C}$ of -60‰, or ~6000-12000 Gt carbon with a -25‰ $\delta^{13}\text{C}$ value (Dickens, 2011). Zeebe et al. (2009) argued that deep sea dissolution records limit the added amount of carbon to ~3000 Gt of carbon and that this amount of carbon could only account for a maximum warming of ~3.5°C. This means that extra unknown process, or processes, must account for the extra warming at the time of the PETM.

Cramer et al. (2003) and Lourens et al. (2005) showed that the temporal distribution of the hyperthermals is in pace with eccentricity scale orbital forcing. However, the precise relation between orbital forcing and the timing of hyperthermals (Lourens et al., 2005; Westerhold et al., 2007; Stap et al. 2009; Hilgen et al., 2010), as well as the exact amount of eccentricity

cycles spanning the gap between H1 and K-Pg boundary is still under dispute (Westerhold et al., 2007, 2012; Hilgen et al., 2010).

Further, the astronomical solution for the Early Eocene is not unambiguous since it is derived from the movement of planets that inhibit chaotic movement. The solution becomes more uncertain the further the solution is calculated into the past and the 400 kyr term cannot be computed with certainty after 60 Ma (Laskar et al., 2011). It is still unclear if the 100 kyr term is reliable for the 50-54 Ma time frame (H. Abels, personal communication).

No final correlation has yet been made between a marine cyclostratigraphic tuned section and the orbital solution because of the uncertainty in the astronomical solution. A successful correlation would establish an absolute time control for the hyperthermals and the Early Eocene.

The PETM was presented for the first time in the continental realm by Koch et al. (1992), and later refined by Bowen et al. (2001). They found a similar CIE derived from paleosol carbonate as the CIE in the marine records, but with a $\delta^{13}\text{C}$ CIE magnitude up to -8‰. Paleosol carbonate nodules record $\delta^{13}\text{C}$ changes because they are formed by CO_2 incorporation of plants by photosynthesis, and therefore, track changes in atmospheric $\delta^{13}\text{C}$ values of CO_2 (Koch et al., 1992).

Only recently the H1 and H2 events have been recorded in a continental section, located within the Willwood formation in the Bighorn Basin, USA (Abels et al., 2012). Abels et al. (2012) presented the Upper Deer Creek (UDC) section that clearly contains H1 and H2 with CIE's of -3.8‰ and -2.9‰ respectively. The Creek Star Hill (CSH) section is a parallel section of the UDC section; H1 and H2 in the CSH section have CIE magnitudes of -3.8‰ and -2.7‰ (van Yperen, 2012). The continental $\delta^{13}\text{C}$ magnitudes during hyperthermals are thus amplified in respect to the CIE's in the marine record.

Abels et al. (2012) found an equal $\delta^{13}\text{C}$ scaling of the H1, H2 and the PETM hyperthermals between the marine and continental realms, suggesting the same origin for these hyperthermals. However, their linear extrapolation does not intersect with the origin. This leads to the strange situation where a CIE is of about -2‰ is present in the continental record when there would be no CIE in the marine records. Therefore, a different relation is needed to explain the observed relation at low or high CIE values, or the equal scaling is erroneous.

A continental record covering new hyperthermals would provide more insight in the relation between marine and continental CIE magnitudes, which is now constrained with only three CIE's. This relation in turn could provide a starting point for answering major questions about hyperthermals. A clear $\delta^{13}\text{C}$ relationship between both realms would be a first step in the definitive understanding of the origin of the carbon needed for hyperthermals. Ultimately, and beyond the scope of this project; a conclusive magnitudes for atmospheric $\delta^{13}\text{C}$ values during hyperthermals might be extracted when the relation between marine and continental isotope values are incorporated in global carbon models. From the $\delta^{13}\text{C}$ values the actual amount of CO_2 release during hyperthermals could be derived.

For these purposes, we extend the Willwood formation section of Abels et al. (2012) upward to seek for the first time, continental equivalents of hyperthermals I1 and I2. The main goal is to infer the relationship between marine and continental $\delta^{13}\text{C}$ excursions.

The Willwood formation in the Bighorn Basin studied by Abels et al. (2012, 2013) is an excellent location to look for

continental hyperthermals. The fluvial deposits of the Willwood formation consists of continuous stacked paleosols and have been intensively studied (e.g. Kraus and Aslan, 1993; Kraus, 1996). Strongly developed paleosols generally alternate with drab colored, weakly developed paleosols. These alternations in paleosol development have been attributed to precessional orbital forcing (Kraus and Aslan, 1993; Abdul Aziz et al., 2008; Abels et al., 2013), or autogenic processes (Kraus, 1987; Hajek et al., 2010). Precessional forcing in the Willwood formation would make it possible to correlate a continental section containing hyperthermals to marine sections with known orbital forcing and hyperthermals in detail.

We establish a sedimentological, cyclostratigraphical and paleomagnetic framework for the interval studied. The $\delta^{13}\text{C}$ record of the older Deer Creek Amphitheater section from Abels et al. (2013) is measured to resolve the long term cyclostratigraphy, and to understand the character of the background $\delta^{13}\text{C}$ variation. The aim of constructing this framework is to infer the relationship between cyclicity and the sediments, and to compare our continental section with records from the marine realm. Further, we perform paleomagnetic research on the interval studied by Abels et al. (2012) that contains a poorly constrained C24r/C24n reversal to improve the position of the C24r/C24n reversal boundary. Eventually, an attempt is made to constrain a cyclostratigraphical framework for the C24r/C24n reversal boundary.

2. Geological setting, background and sections

2.1. Geological setting

The Bighorn Basin is an intramontane basin that subsided due to flexural response to the uplift of the surrounding Bighorn, Beartooth and Owl Creek mountain ranges. The basin was hydrologically open to the north. Uplifting occurred during the Laramide orogeny. The surrounding mountains provided the main source of sediments, but most of the uplift had occurred when the Willwood formation was deposited (Kraus and Riggins, 2007, and references therein). The Absaroka volcanic complex formed in the west after the Willwood formation was deposited (Bown, 1980). A unique and rich fossil record from the late Paleocene to the Early Eocene is recorded in the Bighorn Basin (Gingerich, 2006).

2.1.2. Sediments of the Willwood formation

The sediments of the Willwood formation consist of fine grained alluvium deposited in a floodplain paleoenvironment that have developed into paleosols to various degree. Sedimentation of floodplain deposits is controlled by parent material, groundwater level, vegetation, accumulation rate and climate (Bown and Kraus, 1987). Color banding of the sediments of the Willwood formation in the field is distinct, sediments are red, gray, purple or yellow and can be traced laterally over distances up to 1-2 km. Each paleosol represents one episode of deposition that underwent pedogenesis until the soil formation was abruptly stopped by a new episode of deposition (Kraus and Aslan, 1993). Pedogenesis is primarily controlled by the rate and volume of sediment accumulation and by drainage conditions that cause horizon differentiation (Abels et al., 2013)

and references therein). The degree of paleosol development is derived from color differences, presence and abundance of carbonate nodules, appearance and color of mottling, degree of vertical paleosol development and slickensides (e.g. Kraus and Aslan 1993; Bown and Kraus 1987).

The alluvium in the Willwood formation consists of mudrocks (silt and clay), and sandstones. The sandstone bodies in the Willwood formation show two geometries, a sheet sandstone and a ribbon sandstone (Kraus and Aslan, 1993). Ribbon sandstones form when sand fills a channel that incised in a floodplain (González-Bonorino et al., 2010) or as crevasse splay deposits, while a sheet sandstone forms when the main trunk channel meandered (Kraus and Aslan, 1993). The width/thickness ratio can be used as a quantitative test to distinguish between the two geometries, the width/thickness ratio is 15 or less for a ribbon sandstone and substantially higher (100 or more) for a sheet sandstone. Therefore, the extensive sandstones of 1.5 km wide and more than 10 m thick represent meandering trunk rivers (Kraus and Aslan, 1993).

The Willwood formation can be subdivided into two other main lithofacies (Abels et al., 2013). The second lithofacies are heterolithic, consisting of ribbon sandstones and drab mudrock deposits that represent weakly developed paleosols. The last lithofacies are mudrock deposits with bright colors on which moderate to strongly developed paleosols formed. Because weakly developed paleosols are a consequence of rapid sedimentation those paleosols are attributed to crevasse of the main trunk channel during the avulsion phase of a river system.

The stronger developed paleosols accumulated relatively slowly and episodically. These sediments are deposited during the overbank phase of the fluvial system when sediments are deposited by overbank flooding of the trunk river. Alternation of these overbank/avulsion cycles occurs every 4-10 m. (Bown and Kraus, 1987; Kraus and Aslan, 1993). These overbank/avulsion cycles differ laterally in thickness and pedogenic development, but the variation in thickness seems to be compensated in the next one or two cycles (van Yperen, 2012).

2.1.3. Magnetostratigraphy of the Bighorn Basin

The magnetostratigraphy of the Bighorn Basin has been studied by multiple authors. Clyde et al. (2007) shows multiple sections within the Bighorn Basin to include chron 26 until chron 24, and the polarity pattern in the McCullough peak section is correlated to yield the C24r/C24n reversal (Clyde et al., 1994). Tauxe et al. (1994) correlated their section of the Willwood formation to include the same reversal, and provided an age of 52.8 +/- 0.3 Ma for the top part (chron 24n.1) of the normal chron 24n on the basis of Ar³⁹/Ar⁴⁰ dating. Further, they recognized small-scale anomalies in their section as polarity changes. However, locating the precise boundary is not unequivocal. Clyde et al. (1994) shows a short normal polarity before the main body of the C24n chron and Abels et al. (2012) report a 60 m interval of which no polarity could be determined between the C24r and C24n chrons.

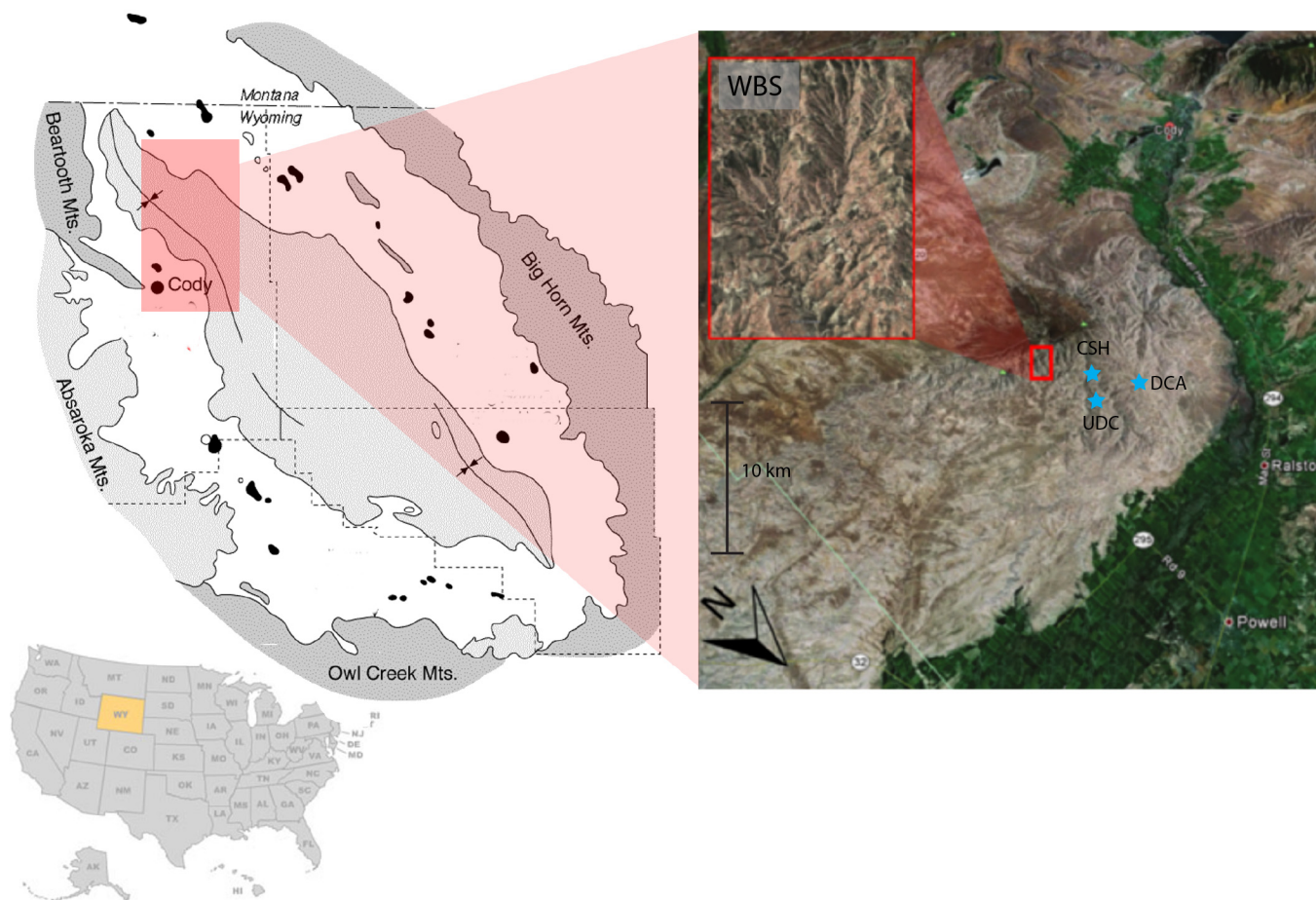


Figure 1: Locations of the sections in the Bighorn Basin. The West Branch section is indicated in red. Creek Star Hill, Deer Creek Amphitheater and Upper Deer Creek are indicated in blue.

2.2. Sections

The West Branch (WB) section is located on the northern edge of the McCullough peaks in the Willwood formation (Figure 1). It has been selected for its height relative to previously studied sections in the area, and the lack of thick sandstone bodies. In total the composite section measures 185.5 m in total and has been logged along four subsections. The base of the section lies 3 m below the distinct purple 4 layer that is correlated to the Wasachian-5 age biozone within the Creek Star Hill (CSH) and Upper Deer Creek (UDC) sections from Abels et al. (2012). The Deer Creek Amphitheater (DCA) section described by Abels et al. (2013) overlaps with the CSH and UDC sections in the upper part and correlates to the Wasachian-4 age biozone.

3. Methods

3.1. Sedimentological description

The WB section was logged in detail after digging ~1 meter wide trenches onto fresher rock. Thickness was measured using a Jacobs's staff. Logged sedimentological features were grain size, color of the matrix, mottling (color, type and abundance), abundance of slickensides, abundance of nodules and remarkable characteristics. Field observations were based on the *field book for describing and sampling soils* (Schoeneberger et al., 2002) and color description was performed by comparing fresh hand samples to the Munsell Color Chart. In addition, every 12.5 cm the color reflectance spectrum was measured on the matrix from fresh rock with a hand held Minolta CM 600. Carbonate nodules were collected from the trenches when present and attributed to 12.5 cm stratigraphic horizons.

3.2. Carbon isotope data

The carbonate nodules were cleaned described and hand grinded to powder by using a mortar and pestle. Spar minerals were carefully left out during grinding. Carbon and oxygen isotopes were measured by a VG SIRA24 EM mass spectrometer with ISOCARB and offline preparation vacuumlines at Utrecht University. The international (IAEA-CO-1) standard was used to determine analytical precision and measured three times every 32 samples. The Utrecht University in-house (NAXOS) carbonate standard was used to correct for the error caused by the use of one acid fluid for 44 measurements. The NAXOS standard was measured 12 times distributed between 32 samples. The resulting isotope ratios are depicted relative to the Peedee Belemnite standard as $\delta^{13}\text{C} = (R_{\text{sample}}/R_{\text{standard}} - 1) * 1000 \text{ ‰}$.

3.3. Principal component analysis and spectral analysis

Principal Component Analysis (PCA) was performed in Past (Hammer and Harper, 2001) using the correlation option for the matrix for the eigenvalue calculation. The values of the loadings were determined using the correlation option since the units of the different variables are non-uniform.

Analyseries (Paillard et al., 1996) and the Redfit (Schulz and Mudelsee, 2002) option in Past were used for the spectral analysis of the isotope data and color data (lightness and redness). In Redfit we used a rectangular window, an oversampling of 2 and 3 segments and the significance was tested with a 99% chi test. For Analyseries the Blackman-Tukey and Bartlett windows

were applied with a 90% certainty interval on the isotope data. For the color data the Bartlett window was used with a 90% certainty interval. Bandpass filtering and equal scaling of the isotope records for the moving averages was performed with Analyseries.

3.4. Paleomagnetism

A total of 88 samples were drilled at an average sample level of 1.3 m between -19 m and 64 m and at a 4 m average between 64 m and 176 m. 70 samples were selected for thermal demagnetization (TH). Thermal demagnetization was performed in a magnetically shielded furnace with temperature increments of 50°C-100°C for the first 200°C followed by smaller steps of 20°C-40°C towards 710°C. The natural remanent magnetization (NRM) was measured with a 2G Enterprises DC SQUID cryogenic magnetometer with a noise level of $3 \times 10^{-12} \text{ Am}^2$. Resulting Zijderveld projection diagrams (Zijderveld, 1967) were interpreted using PCA analysis (Kirschvink, 1980). All resulting directions are given without tectonic correction since the bedding was practically horizontal.

4. Results

4.1. Sedimentology

A detailed logged WB section is presented in Figure 2. The Willwood formation has been described extensively. Therefore, we will merely outline the major sedimentological features. We follow Abels et al. (2012) and divide the sediments in heterolithic and mudrock deposits. The extensive sheet sandstones described in the Willwood formation are not present in the WB section.

4.1.1. Heterolithic deposits

Heterolithic deposits consist of mudrocks interbedded with channel sandstones. The sandstones are up to 3 m thick and consist of very fine to fine sandstone with a white, gray or a greenish color. Most sandstones can laterally be traced over several hundreds of meters, although some pinch out after less than tens of meters. Up to cm-scale bedding can be present, sometimes highlighted by iron oxides or other fine grained components. The bases of the sandstones are either sharp when bordering well-developed paleosols or coarsening upward when coarser grained material is overlain. Sandstones can show light pedogenesis in the form of nodules or a small amount of mottling.

The mudrocks range from clay to siltstone. Colors are usually brown and gray (5YR 4/4 or 5YR 3/3 and 10GY 5/1 or 5G 5/2) with occasionally yellow (2.5Y 6/6). Evidence of weak pedogenesis include burrows, mottles (often being rhizolites), slickensides and either carbonate or iron oxide nodules. Very rarely dewatering fractures are present.

Thicknesses of the paleosols differ from decimeter-scale to a meter-scale, the total thickness of a simple mudrock sequence ranges from 0.2 to 5.0 m. The boundaries between different levels of sediments can be very clear, with rapid changes in composition (see m. 57, Figure 1) or indistinct, where the boundary is hazy (see m. 85 Figure 1). In general, the latter occurs more often than the former.

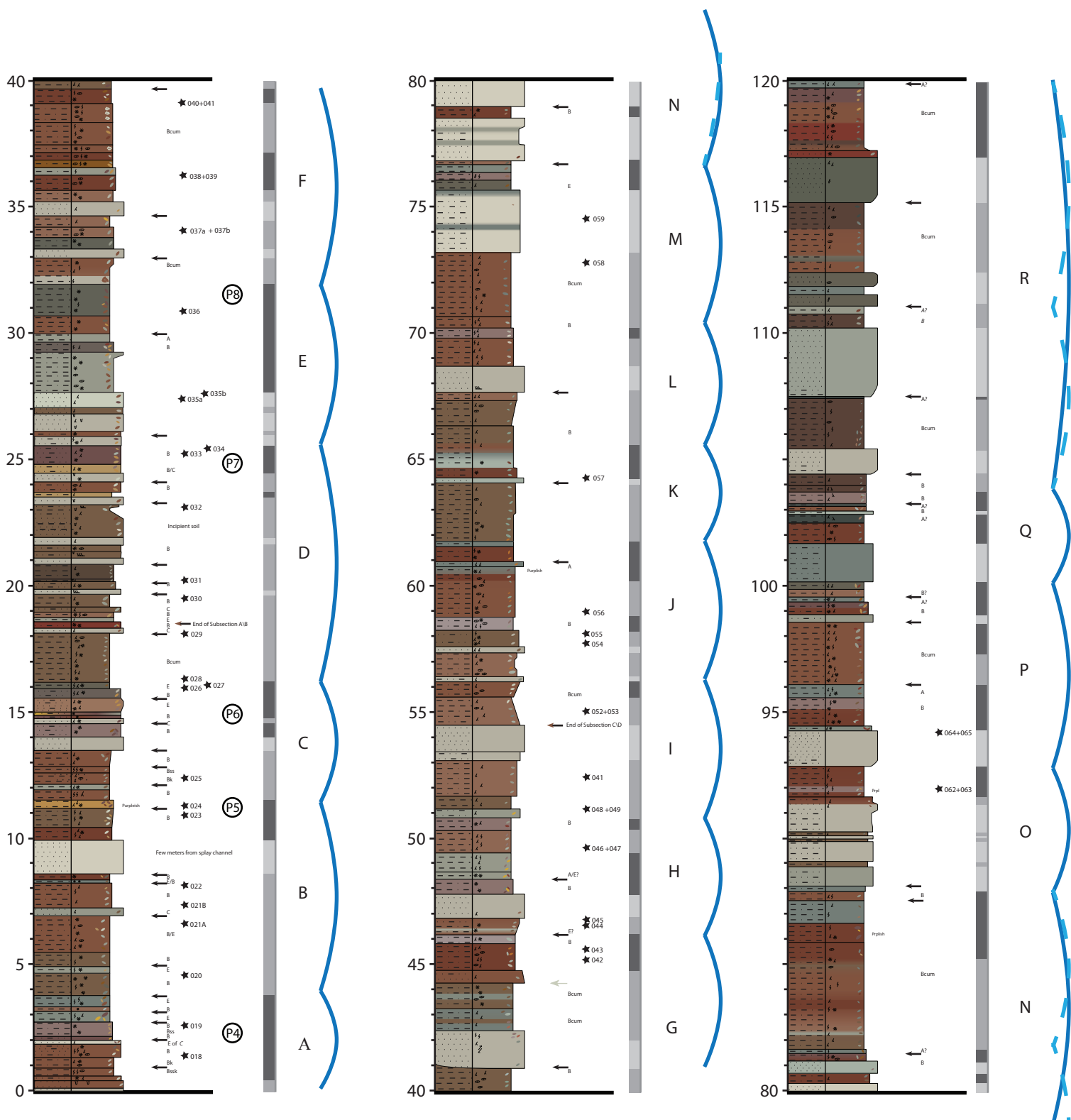
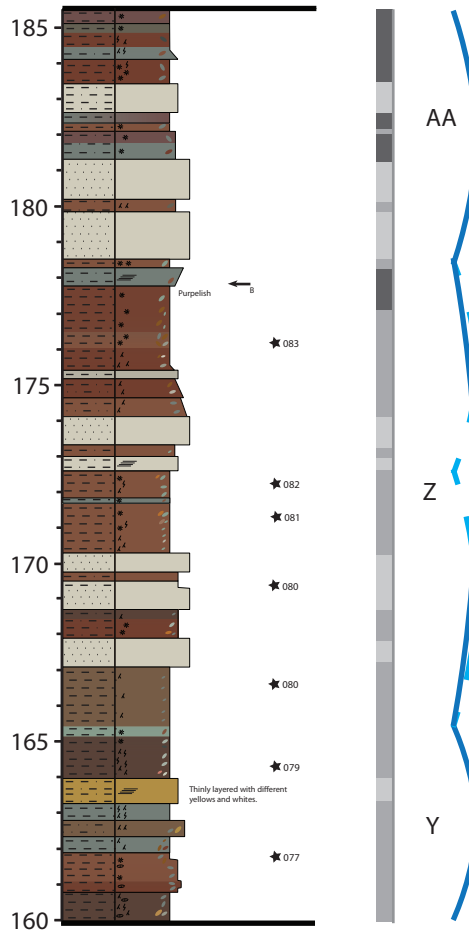
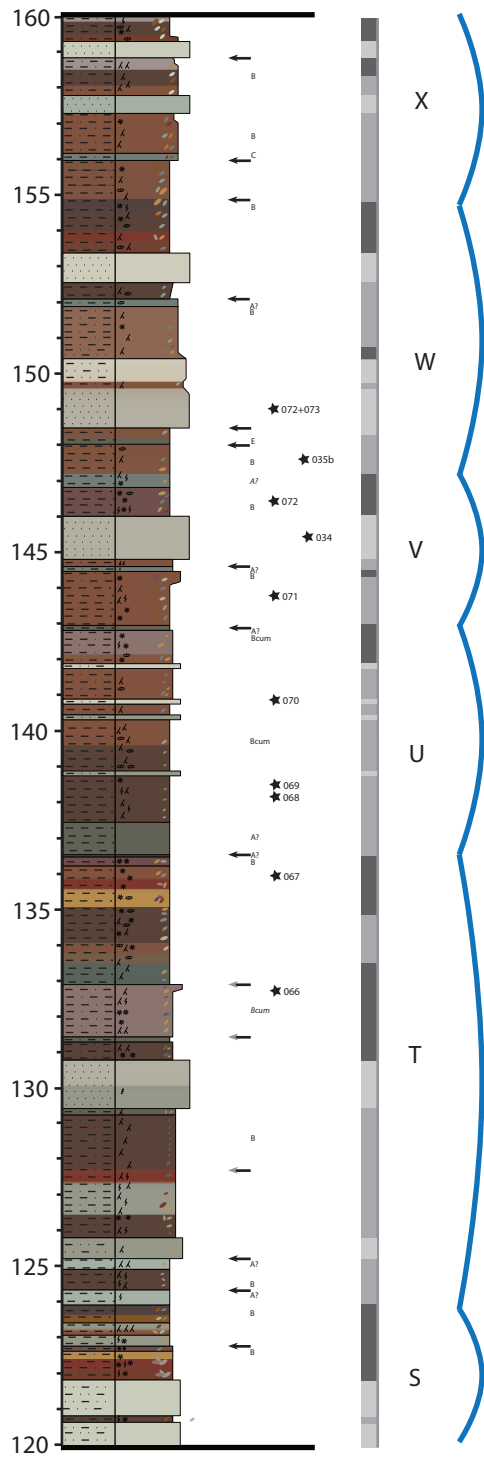


Figure 2: Simplified field log of the WB section showing bed thickness and induration, color, grain size, matrix color and features as slickensides, mottling (and its color) and the presence of nodules. If features were abundant this is indicated by drawing multiple signs. The top of a soils is marked with an arrow, in the lower 25 meter this is indicated more often than in the upper part of the section. Clear purple layers have been labeled according to Abels et al. (2012). The degree of paleosol development is based on Abels et al., 2013. Blue lines indicate avulsion/overbank cycles based on the paleosol development, dotted lines are options for the division of thick cycles N, R and Z.



Legend

9GY 7/1	5G 6/2	↵ Burrows
5Y 7.5/1	10GY 4/1	∧ Roots
10Y 7/1	7.5YR 5/7	* Roots
5YR 4/4	10YR 5/7	⊙ Nodules
2.5 Y 6/6	7.5R 4/2	⚡ Slickensides
7.5YR 4/1	10R 6/1 "Light Purple"	Mottling
10Y 5/1-2	10GY 8/1	Many Mottling
"Dark Purple" - 7.5R 3.5/2	5G 3/1	Patchy Mottling
2.5Y 6/4	5YR 3/2	★ PMag sample
9GY 5.5/1	10Y 7/1 more green	≡ Cross bedding
5YR 4.5/3	10R 3/1	⧱ Small (dehydration) faults
7.5YR 4/3	10R 6/6	≡ Laminated soil
2.5YR 3/4		← Top Paleosol
7.5YR 5/3		█ Intense developed paleosol
10R 3/5		█ Weak developed paleosol
7.5YR 3/2		█ No paleosol development
	Grain size:	
	(Very) Fine sandstone	
	Sandy silt	
	(Muddy) Silt / Silty mud	
	Mud / Clayey mud	

4.1.2. Interpretation of the heterolithic deposits

The degree of pedogenesis in the heterolithic horizons is low, although some pedogenic features such as mottles and nodules are present. The fine grained brown/red deposits are interpreted as B horizons and thick horizons as B stacked paleosols (Kraus and Aslan, 1993). Usually no other paleosol horizons can be outlined since the vertical soil profile development is weak. Another indication for the incipient paleosols are the drab colors of the sediments (Bown and Kraus, 1987). The deposits can most probably be attributed to the immature stages (stage 1 and 2) of soil formation from Bown and Kraus (1987). These soils are developed weakly because sediment accumulation is relatively rapid, which does not leave enough time for minerals to leach and accumulate (Kraus and Aslan, 1993). Therefore, the heterolithic sediments are interpreted as concurrent with the avulsion phase of a fluvial depositional system (Kraus, 1996; Abels et al., 2013).

4.1.3. Mudrock deposits

The decimeter to 0.5 meter thick mudrock paleosols comprise of claystones to sandy siltstones, although the coarser grain sizes are rare. Colors include red (10R 3/5), brown (5YR 3/2), yellow (2,5Y 6/4), purple (10R 6/1), greenish and dark gray (5G 6/2 and 10GY 4/1). Vertical paleosol profile development is strong. The deposits are decimeter to half a meter thick and laterally very homogenous. For example, the prominent purple 4 layer (P4, Figure 1) can be traced over a few kilometers. Slickensides, carbonate nodules and pervasive mottling (rhizoliths) are often present in the paleosols. The mottling has clear red, yellow or purple colors. The boundaries of these horizons usually have very distinctive, sharp contours (see meter 120, Figure 1).

4.1.4. Interpretation of the mudrock deposits

Pedogenesis in the mudrocks is relatively high. Deposits can be divided in A, B, Bss, Bssk, and sporadically E and C soil horizons. The A horizons embody a gray matrix with mottles. The B horizons are either purple, red, dark brown or a mixture of these colors, including intense mottling and often clear horizon boundaries. Especially the purple horizons are clearly distinguishable and described as paleo B-horizons (Kraus and Aslan, 1993). Thicker mudrock deposits are assigned to mature stage 4 deposits while thinner cumulative paleosol mudrocks are judged as moderately mature (stage 2+ or stage 3) (Kraus and Aslan, 1993).

Slower sedimentation rates accounted for the formation of distinct paleosols, allowing for the time that soils need to mature. We interpreted the mudrocks as overbank deposits that have been deposited during sedimentation pulses that were either sporadic or low volume influxes.

4.2. Pedogenic maturity

All paleosols represent a certain pedogenic degree. Bown and Kraus (1987) constructed their five stages of paleosol maturity on the basis of horizon thickness, vertical profile, color, and the presence of nodules and mottling. Vertical and horizontal relationships between the soil horizons can be resolved using the soil maturity. Abels et al. (2013) calculated a Soil Development Index (SDI) from the soil properties and divided the soils in three stages; no pedogenesis, weak pedogenesis

and intense pedogenesis. Corresponding SDI values in the same rising order are 0-0.5, 0.5-1 and 1-2. A detailed approach of calculating all the SDI values per paleosol was beyond the scope of this project. However, we generalized the idea of Abels et al. (2013) to be able to attribute one of the stages of paleosol development to the WB section. In the section from Abels et al. (2013), certain types of paleosols are always attributed with the same SDI value. The very clear A horizons, thick bright red paleosols, thick paleosols with pervasive mottling, red paleosols with slickensides and nodules, and purple soils have persistent SDI values of 1-2. In contrary, sandstones never score above 1. We correlate SDI values from the DCA to the WB section since both sections contain the same type of paleosols. Brown and light red paleosols are the hardest paleosols to compare with the paleosols of Abels et al. (2013). Thick brown paleosols that include mottling, roots and nodules (see meter 4-9 in Figure 2) have been interpreted as weakly developed paleosols on the basis of the lack of vertical profile development. Whenever prolific A or purple horizons were present above these thicker brown paleosols (see meter 45 in Figure 2), the brown horizons were interpreted as the B horizon of a strong developed paleosol. Using these criteria a substantial part of the WB section could be related to a pedogenic degree.

4.2.1 Cyclicity in the paleosol maturity

Looking at the soil maturity pattern that emerges from Figure 2, in general an intense pedogenic developed interval overlies a thicker soil with weaker pedogenic development. These 27 alternations have been marked in blue and labeled with a letter each (Figure 2). The top of an alternation has been placed at the top of the intense developed paleosol, as in agreement with Abels et al. (2013). The cyclic alternations can be very clear as in cycle B, C, D, G, P and U, or less clear as in cycle F, H, I, J, O, W, Y, Z and AA. Cycles can have distinct paleosol horizons but nonetheless cycle boundaries can be hard to define, as example with cycle T. Some cycles can be recognized directly in the field as with cycles S, T and partly R (Figure 3). The soil does not show clear horizons in abnormal thick cycles R and Z, these cycles probably consist of more than one cycle (shown in dotted lines in Figure 1). Thicknesses of the cycles (without R and Z) range from 3.5 to 12.4 m thick.

The average thickness including cycles R and Z is 7.0 m with a standard deviation of 3.1 m. When excluding cycle R and Z the average thickness is 6.4 m, with a standard deviation of 2.2 m. Cycle T and N are also relatively thick and might also contain more cycles but no real indications for extra cycle boundaries are present in the lithology. Cycle A has not been included in any consideration since the lower boundary is unclear.

4.2.2. Interpretation of the lithological alternations

The lithological cycles are interpreted as an alternation of periods with rapid sedimentation followed by periods with a slower accumulation rate. During periods with slower sedimentation rates well defined paleosol horizons can form, which are overlain by heterogeneous paleosols during faster phases of sedimentation. This implies a non-linear time pattern of sediment deposition. The same mean cyclicity is found in the Polecat Bench and Red Butte sections (Abdul Aziz et al., 2008) with alternations consisting of 7.6 m and 8.7 m, in the UDC section at around 7.0 m (Abels et al., 2012), and in the DCA section at 7.1 m (Abels et al., 2013).

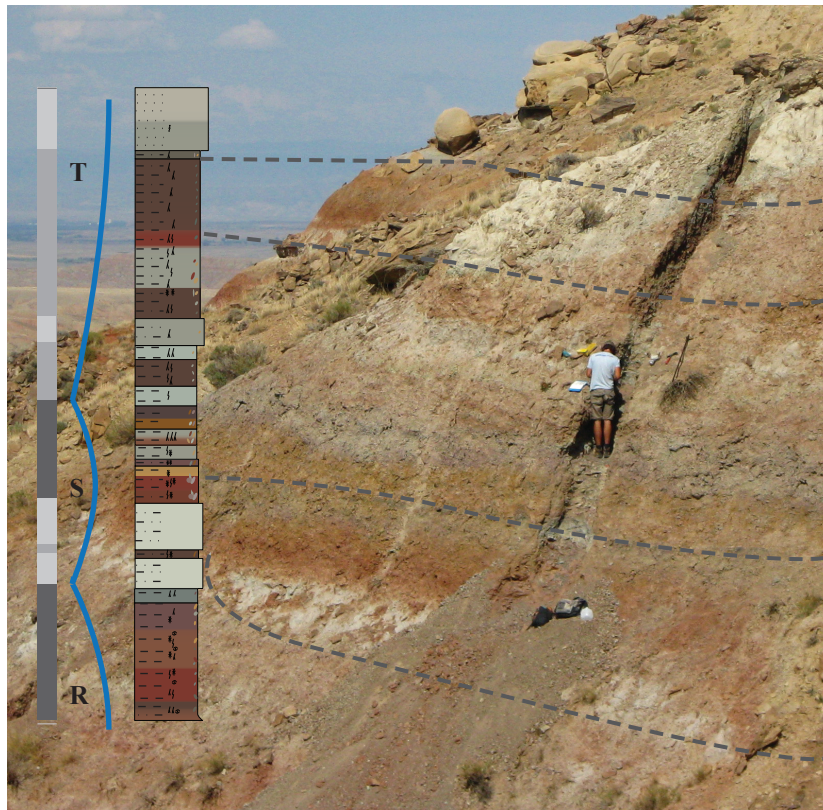


Figure 3: Avulsion/overbank cycles in the field. On the right the field log is indicated, on the left the interpretation of the avulsion/overbank cyclicity. Note that surface colors differ from fresh rock colors due to downwashing of sediments and drying. Cycle R is not drawn on scale. Person for scale.

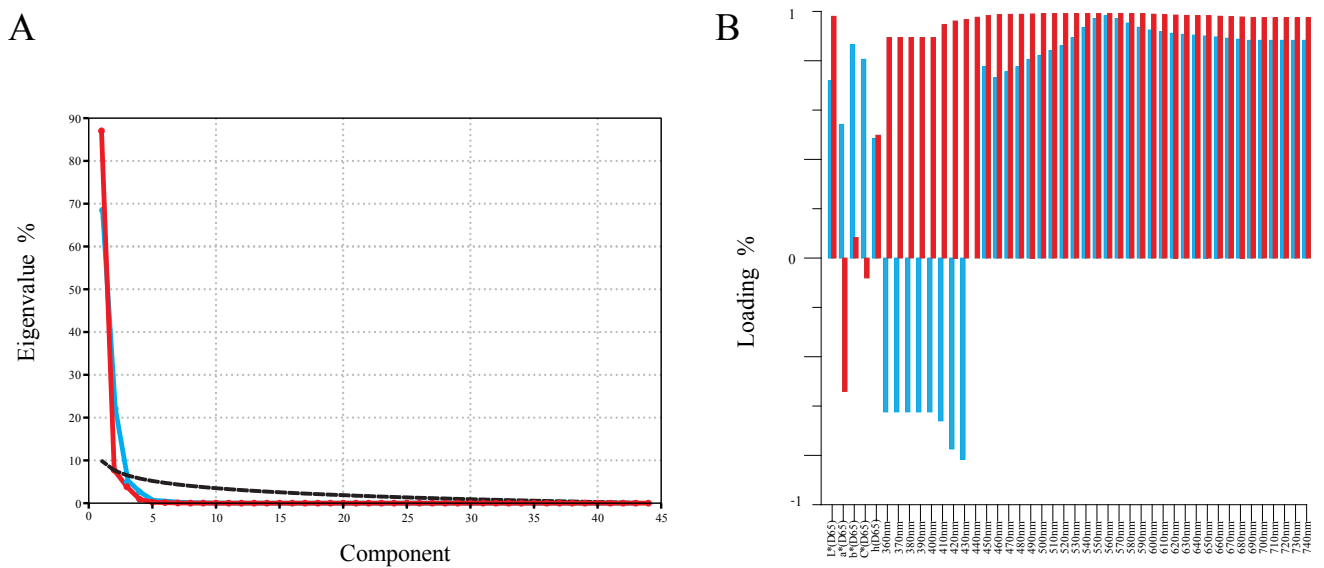


Figure 4: PCA component analysis for the color data (red) and color data normalized to 440 nm (blue). **A:** Scree plot with broken stick cut off (black dotted line). **B:** Loading percentages for the color data.

4.3. Color data, principal component analysis and time series analysis

Output from the color measurements are given in two values for each sample level. The first output is measured with one illuminant; the second measurement uses two illuminants. Both outputs are alike except for the amplitude which is slightly bigger in the first value, which we will work with in this study.

4.3.1. Principal component analysis (PCA)

Color measurements are described to relate to lithology in the Willwood formation (Abdul Aziz et al., 2008; Abels et al., 2012, 2013). Principal component analysis (PCA) has been performed to pinpoint which output parameters of the color measurements represents lithology. Since the PCA finds components that account for the largest variance within the data set, these components might be correlated to underlying

variables like lithology (Davis, J, 1986). A PCA is successful if a few variables account for most of the variance.

The result of the PCA is given in Figure 4a, the first component reflects 87% and the second component accounts for 9% of the variance. Components below the red “broken stick” model can be considered as non-significant (Jackson 1999). Component loading is calculated to show to what degree the original variables contribute to the components. The loading of variables for the first component (Figure 4b) shows that apart from the wavelengths itself, the lightness (L^*) and redness (a^*) highly contribute to the first component. Redness has a negative loading, implicating that the redness is in anti-phase with the other variables. The correlation between the high loadings for the lightness and the wavelengths is expected since lightness is defined as the area under the visible light wavelengths spectra curve (Balsam et al., 1999). The data is normalized to the 440 nm wavelength to correct for the high influence of lightness (Abels et al., 2013). No color property from the normalized data that can be linked to variance stands out (Figure 4b).

The lightness and redness both clearly follow lithological changes (Figure 5). The lightness is highest when sandstones or light A paleosols are present, occasionally bright yellow horizons are also distinctly marked in the lightness. The red horizons give different lightness values, but do not stand out in the overall pattern.

In contrast to the lightness, the redness gives a “square like” graph when compared to the stratigraphy (see values around 165 m). With peak values at red horizons within a range such that vertically, almost straight lines are the result. This feature is less clear in the lower part of the section. Redness is zero, or close to zero when light sandstones are measured. Regarding the PCA and the relation of the lightness and redness with the lithology, lightness and redness can be considered within certain limits, a proxy for lithology.

4.3.2. Time series analysis of the color data

We use Blackman-Tukey (Blackman and Tukey, 1958) and Redfit (Schulz and Mudelsee, 2002) power spectra analysis on the lightness record to extract cyclic patterns in the lithology of the WB section (Figure 6a-d). For the lightness the Blackman-Tukey spectra with Bartlett window and 90% certainty show a power spectrum peak between 3.85 and 8.5 m and multiple peaks below 3.5 m. The Redfit spectra using a 99% chi square test show peaks at 3.6 m and 5.3 m. For the redness with the same certainty, the Blackman-Tukey with Bartlett window spectra shows more distinct peaks between 3.4-3.8 m, 3.8-4.4 m, 4.8-5.8 m and 5.8-9.3 m. The Redfit spectra show an extra 7.1m peak in comparison to the lightness record.

4.3.3. Bandpass filtering of the color records

A bandpass filter is applied to both the lightness and redness records to pinpoint the cyclic patterns in the overbank/avulsion pattern. As the thinnest overbank/avulsion cycle is 3.7 m, only wavelengths of 3.7 m or greater are considered within this study. The lightness and redness bandpass filters have been given a frequency between 3.7 and 10 m (Figure 5). Overall the redness and lightness show the same pattern but the redness has a greater amplitude at ~0 and ~45 m. The lightness record shows a less distinctive pattern, and has a greater amplitude in the top of the section compared to the lower part. The bandpass filter for the lightness indicates 35 cycles with 5

optional additional cycles, while the bandpass filter for the redness indicates 34 cycles with 6 optional additional cycles. The difference with the interpreted cycles from the lithology with the lightness and redness is respectively eight and seven. Differences are very clear in the thicker cycles N, R, T and Z. These cycles are thicker than the maximum frequency of the bandpass filter and probably hold more than one cycle (Figure 5). As an example, the thickest cycle (R) shows three cycles in the bandpass filter for both lightness and redness. To circumvent this problem, the total amount of cycles in the section has been calculated with the assumption that the thick cycles actually consists of thinner cycles that have mean thicknesses (e.g. 7.0 m). Together the four thick cycles are 52.6 m and following this assumption would then contain 7.5 cycles. The section would then include a total of 30.5 cycles, which is closer to the 34 cycles present in the redness bandpass filter. It is very likely that the thin sandstone layers that have high lightness values have a substantial influence on the bandpass filter since the smallest cycles are of the same order of thickness as sandstone layers, resulting in a too short wavelengths of the lightness and redness bandpass filter.

4.4. Paleomagnetism

Demagnetization diagrams for indicative samples are given in Figure 7. Interpretation and direction of the samples are listed in Appendix 1. Zijderveld diagrams with three distinguishable components (Figure 7a and 7b) result in clear polarity signals. The first component is demagnetized between 100 and 240-270°C and is considered the present day field overprint, which is present in the majority of samples. The second component unlocks in the temperature interval of 270°C-540°C. This component has a slightly different direction than the overprint (Figure 7c). In Figure 7c, this small direction change in the Zijderveld diagram is visible at 270°C. The Characteristic Remanent Magnetization (ChRM) begins to unlock as third component in the highest temperature range between 510-570°C. The Zijderveld diagrams given in Figure 7c show the removal of the second component with a normal direction followed a reversed signal (Figure 7d). This third component represented by these reversed measurements is considered to be the ChRM (see detail, Figure 7d).

Other samples only show the overprint and a second component, which does not decay towards the origin (Figure 7e, 7f). We label this component Unidentified Component (UC). A UC can either resemble a ChRM with lower unblocking temperatures or a second component as in Figure 7c.

26 of the 70 samples did not indicate meaningful ChRM directions or could be characterized as UC. Examples are: Samples that have random directions (7g), they were incorrectly orientated (7h), or samples do not carry a signal after being exposed to intermediate temperatures (around 480°C, Figure 7i). Samples were considered to reach noise level when intensities fell below 100 A/m².

Equal area plots with mean directions of the different components are given in Figure 8. The present day overprint is expected to have a declination of 0° and an inclination of 63° (purple dot in Figure 8a) (Clyde et al., 2007), while the mean overprint direction is 349° (declination) and 67° (inclination). This indicates that not all data in the lower temperature range (100-240°C) are the exact present day overprint. The poor quality of the data is likely to cause this offset.

Expected Eocene declination and inclination for the Bighorn Basin based on the Eocene reference pole for North

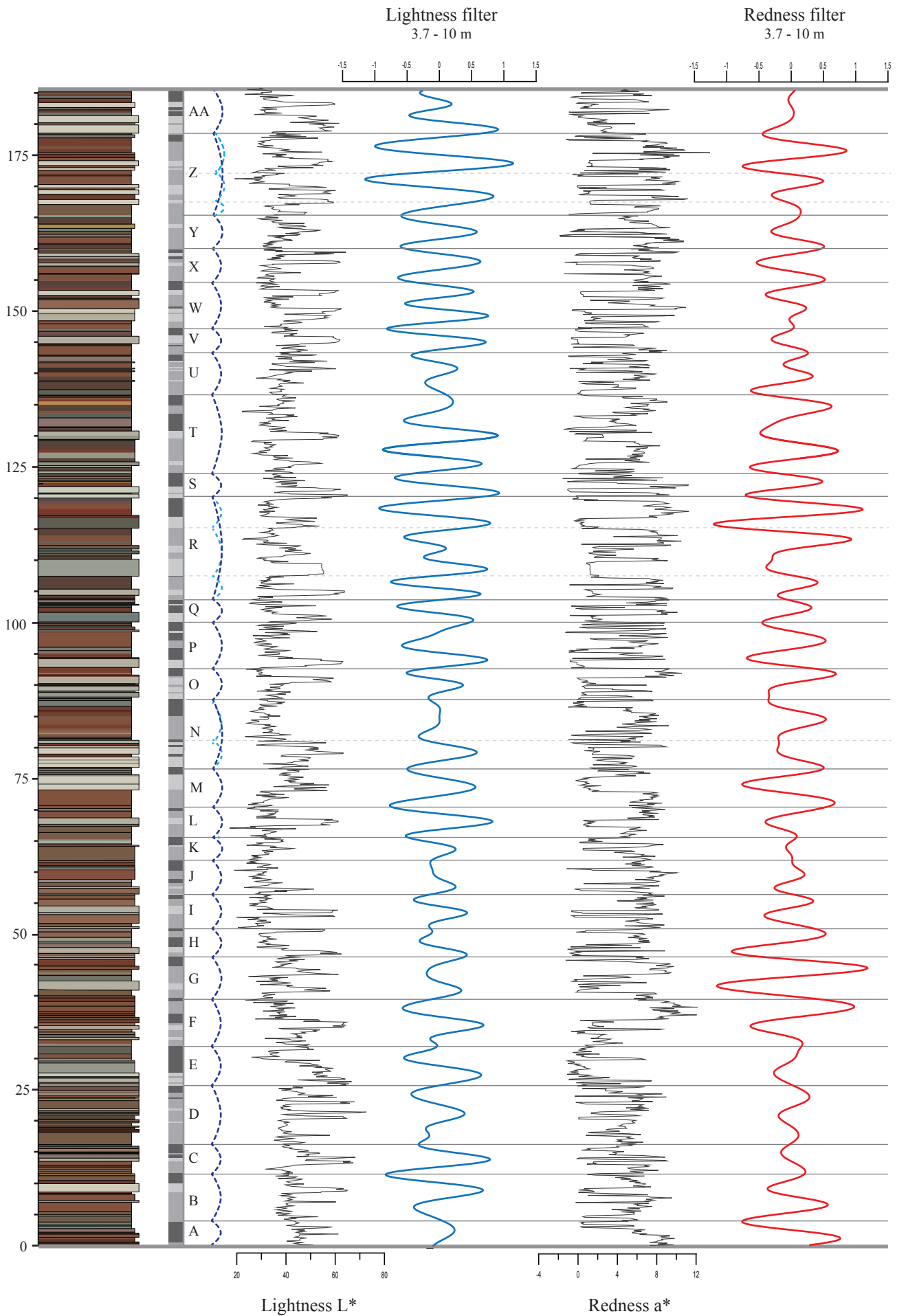


Figure 5: Color data against lithology. Shown from left to right are: a compact version of the field log, the avulsion/overbank cycles, lightness (L*), the 3.7 - 10 m bandpass filter of the lightness data (in blue), redness data (a*) and the last red line is the 3.7 - 10 m bandpass filter of the redness data.

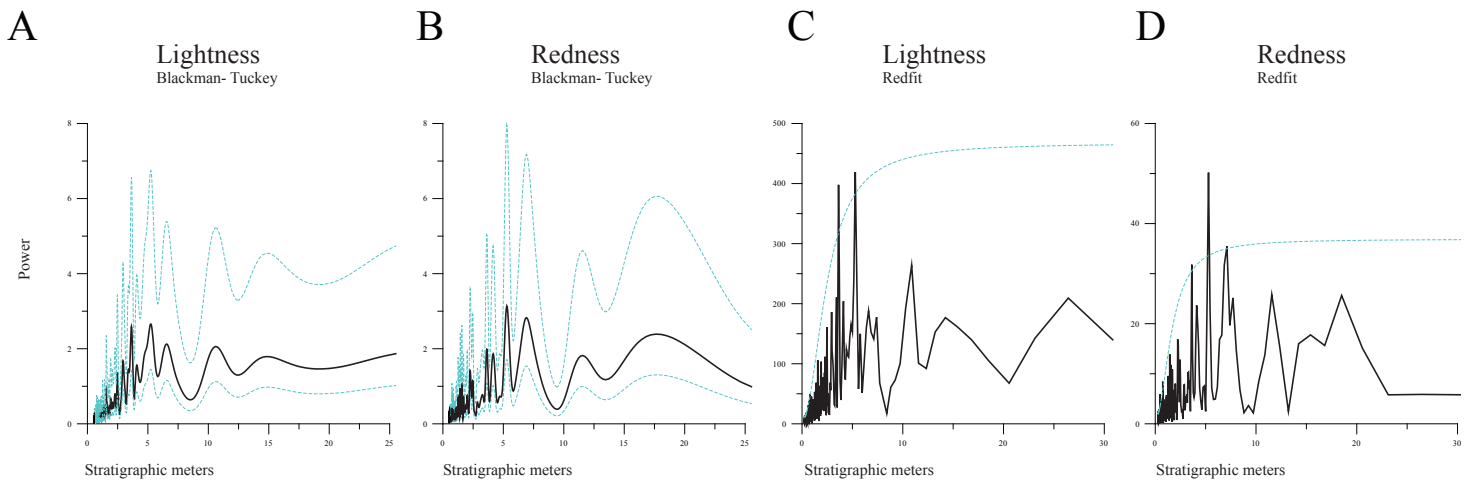


Figure 6: Blackman-Tukey and Redfit spectral analysis for the redness and the lightness records. For the Blackman-Tukey plot, the blue lines are the 90% certainty interval significance spectra. For the Redfit plot, the blue line is the 99% chi significance cut off.

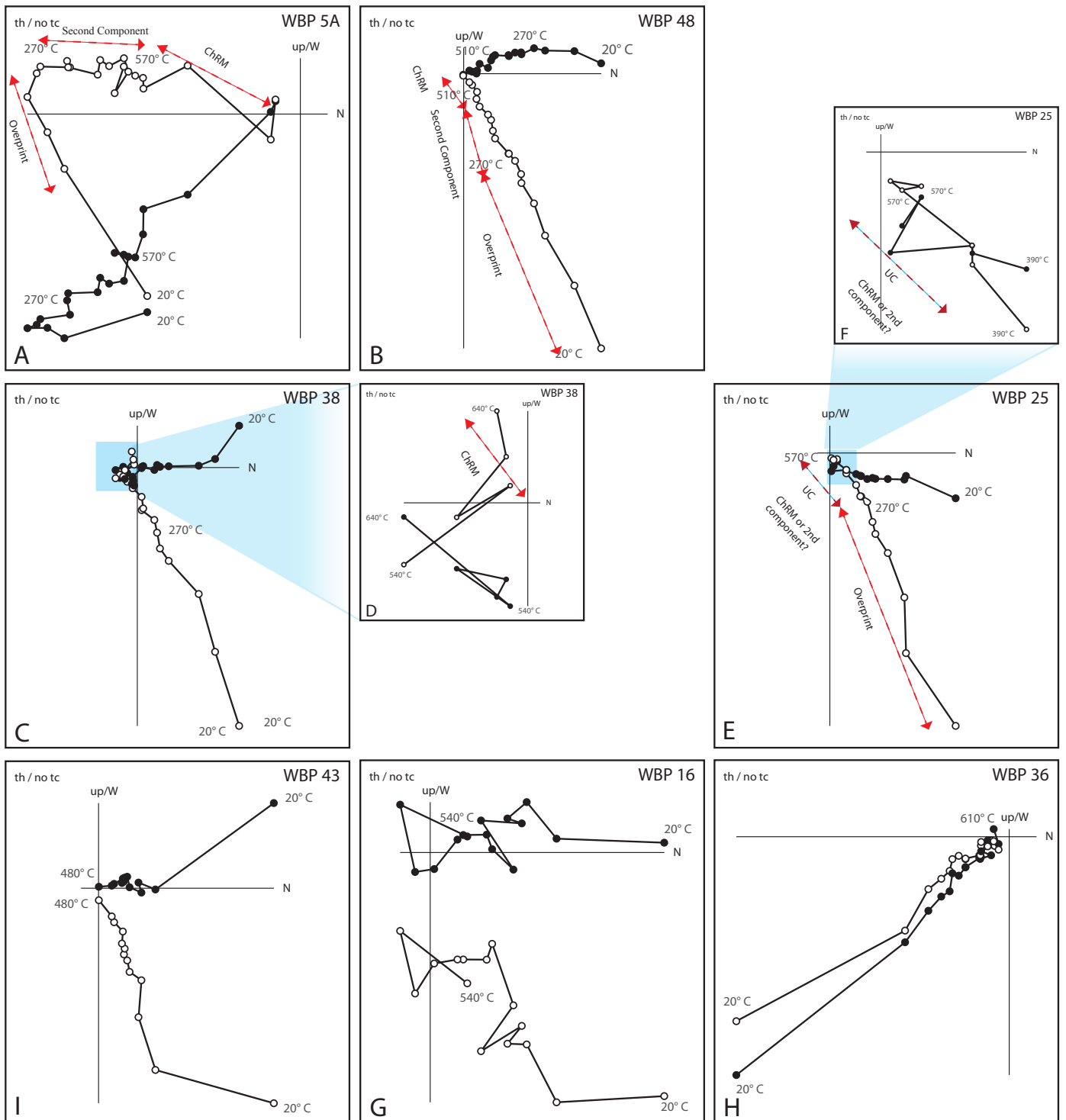


Figure 7, page 16: Zuiderveld diagrams of indicative samples. **A:** A sample with 3 components with a reversed ChRM. **B:** A three component normal ChRM. **C:** A hard to distinguish reversed ChRM. **D:** Magnification of the reversed points of plot C. **E:** Sample with a Unknown Component. **F:** Magnification of the last points of the UC. **I-G:** Examples of diagrams that could not be interpreted as meaningful directions.

America (Diehl et al., 1983), are respectively 349° and 63° (pink dot in Figure 8b). The mean normal ChRM direction is 332° for the declination and 68° for the inclination. Compared to the expected directions the ChRM is about 17° off for the declination and about 4.5° too steep for the inclination. However, the validity of the primary origin of the ChRM is supported by the antipodal mean normal and reverse ChRM directions. Reverse directions in the second component equal area plots have very high mean α_{95} value and both the second component and ChRM equal area plots show a large scatter in reverse data points. This can be explained by the type of sample that shows a Zuiderveld plot that starts with data in the normal quadrant and moves in the reversed quadrant (Figure 7c). In these reverse samples, the directions are inferred from only a few points with some data points still in the process of losing their normal overprints. This results in a direction that is not the isolated reverse direction but is largely influenced by overprints.

To establish which normal UC data represent a ChRM, we compare the α_{95} of the ChRM and second component means

with the UC data (Figure 8d). If UC data falls within the mean ChRM α_{95} range it can be considered ChRM. Reversed UC components have not been considered due to low amount of reverse UC and second components in the samples. Two data points can be pointed out as lying in the ChRM and outside the second component mean α_{95} range. However, since only two of the second component data points lie within the α_{95} range it is at least considered as doubtful to use this method.

The CSH and UDC sections have previously been sampled and measured for paleomagnetic research. Samples from the CSH and UDC sections show similar magnetic behavior as the samples presented here and have been reexamined for this study. Only clear ChRM directions that show as a third component in a sample have been taken into account since not all samples from the CSH and UDC sections have been treated to such high temperatures that all Natural Remanent Magnetization is removed.

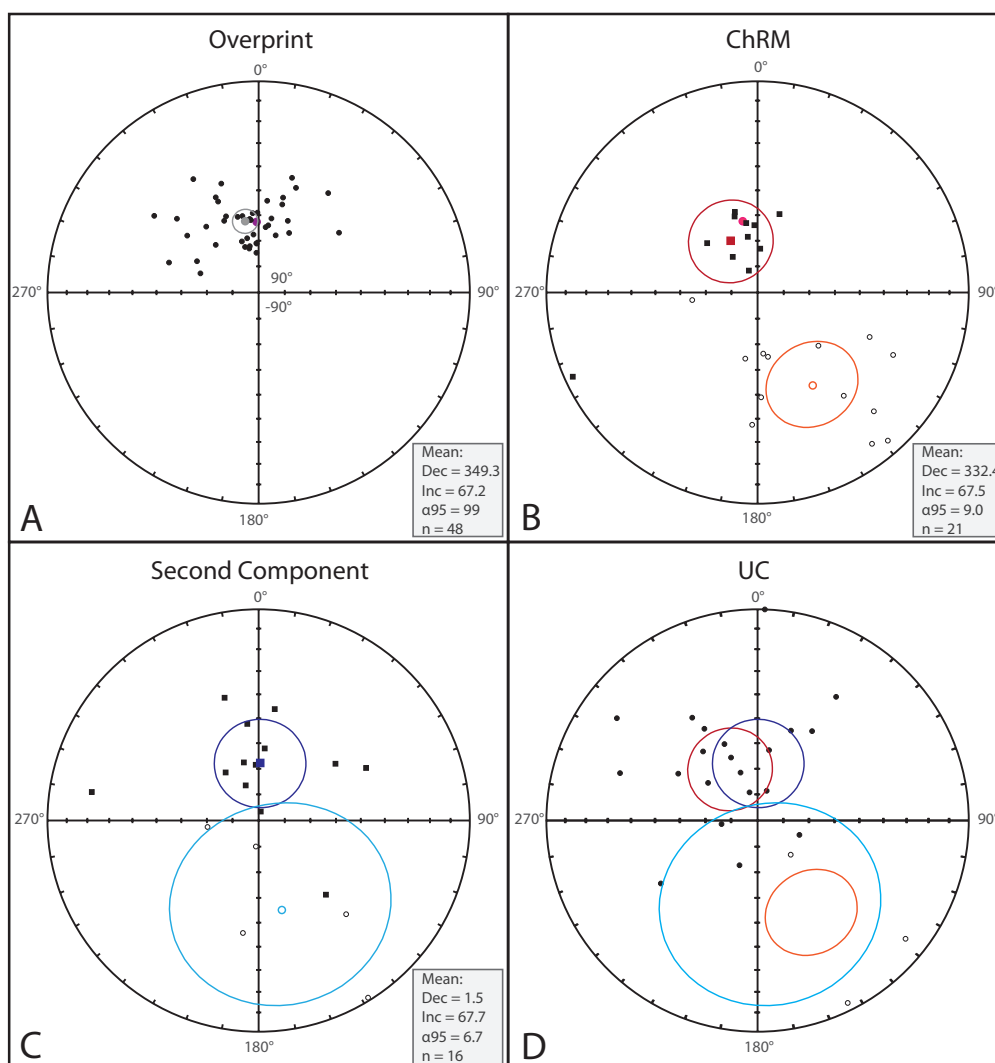


Figure 8: Equal area plot diagrams for the overprint (A) with expected overprint direction in purple, ChRM (B) with expected paleopole direction indicated in pink, secondary component (C) and type UC (D). The α_{95} values of the ChRM (blue) and secondary components (red/orange) have been plotted in the UC plot.

4.4.1. Polarity pattern

The polarity pattern is based on the ChRM directions and is shown in Figure 9, the UC are also plotted. The polarity pattern can be separated into two parts, below ~47 m the section is reversed with two thin normal intervals while above ~47 m the polarity is normal. Of the lower thin normal polarity no lower boundary can be deduced. The upper thin normal polarity is minimal 10.4 m, and maximal 22.1 m thick. The thin normal intervals are only recorded by the WB section; no samples that were interpretable from these intervals are present in the CSH and UDC sections.

The paleomagnetic results from the UDC and CSH are plotted next to the WB section in Figure 8. The purple layers which can be traced in all sections are used to tie the location of the paleomagnetic samples to the WB section (Abels, personal communication). Since the normal polarity samples of the UDC section are positioned ~25 m above P7 a good correlation between the normal samples in the top of the section of the WB and UDC is lacking. Therefore, the normal polarity samples of the UDC section are not used to refine the main reversal at ~47m. The correspondence of the shift from reversed to normal directions in the WB and UDC sections is striking.

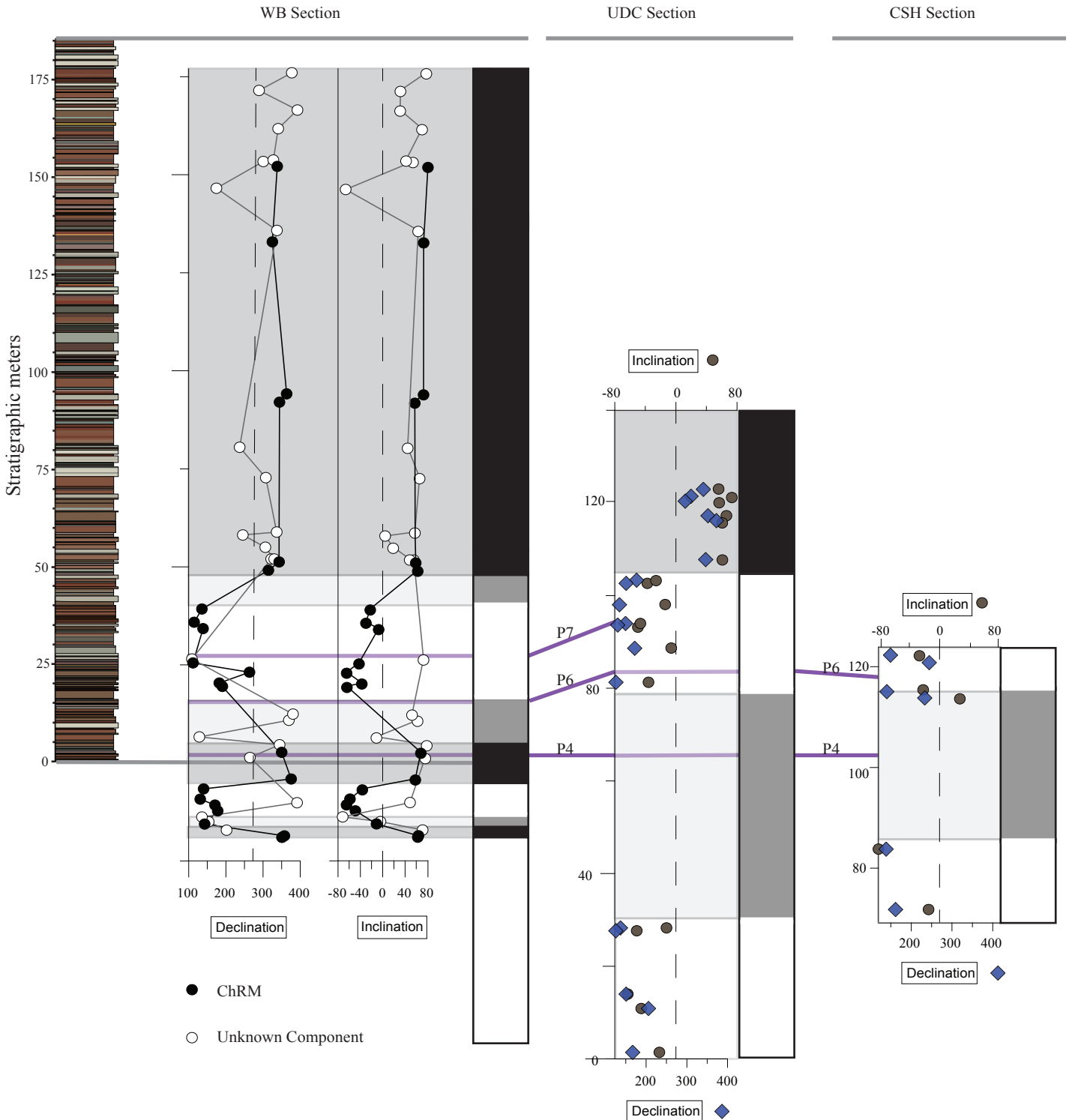


Figure 9: Paleomagnetic results. For the WB section the black dots indicate ChRM directions, while the white dots indicate the Unknown Component directions. For the UDC and CSH section, blue marks are declination and brown marks are inclination, no UC is shown for these sections. The sections are linked on the basis of the distinct purple layers, purple 4,6 and 7 are indicated in purple.

4.5. Carbon nodule isotope data

Carbon and oxygen isotope measurements of micritic carbonate from the WB and DCA section are listed in respectively Appendix 2 and Appendix 3. Measurements of diagenetic spar samples per section can also be found in the Appendices 2 and 3.

A total of 239 carbonate nodules have been measured from the WB section from 213 stratigraphic levels, 26 levels include two nodule measurements. The carbon isotope measurements span from -14.13‰ to -8.18‰, while oxygen

isotopes measurements range from -11.31‰ to -7.29‰, both are plotted in stratigraphic order in Figure 10a. The characteristic $\delta^{13}\text{C}$ variation between nodules from the same stratigraphic level is given by the mean standard deviation for the difference between nodules per level, which is 0.29‰ (n = 26). The isotope data below 0 m has been provided by Van den Berg (2012).

A total of 238 nodules have been measured from the DCA section, collected from 150 stratigraphic levels. From 81 levels two nodules have been measured twice, and 7 levels include measurements of three nodules. $\delta^{13}\text{C}$ measurements ranged from -12.94‰ to -7.51‰ and $\delta^{18}\text{O}$ measurement varied within -10.31‰ and -7.46‰. Figure 10b shows the measurements

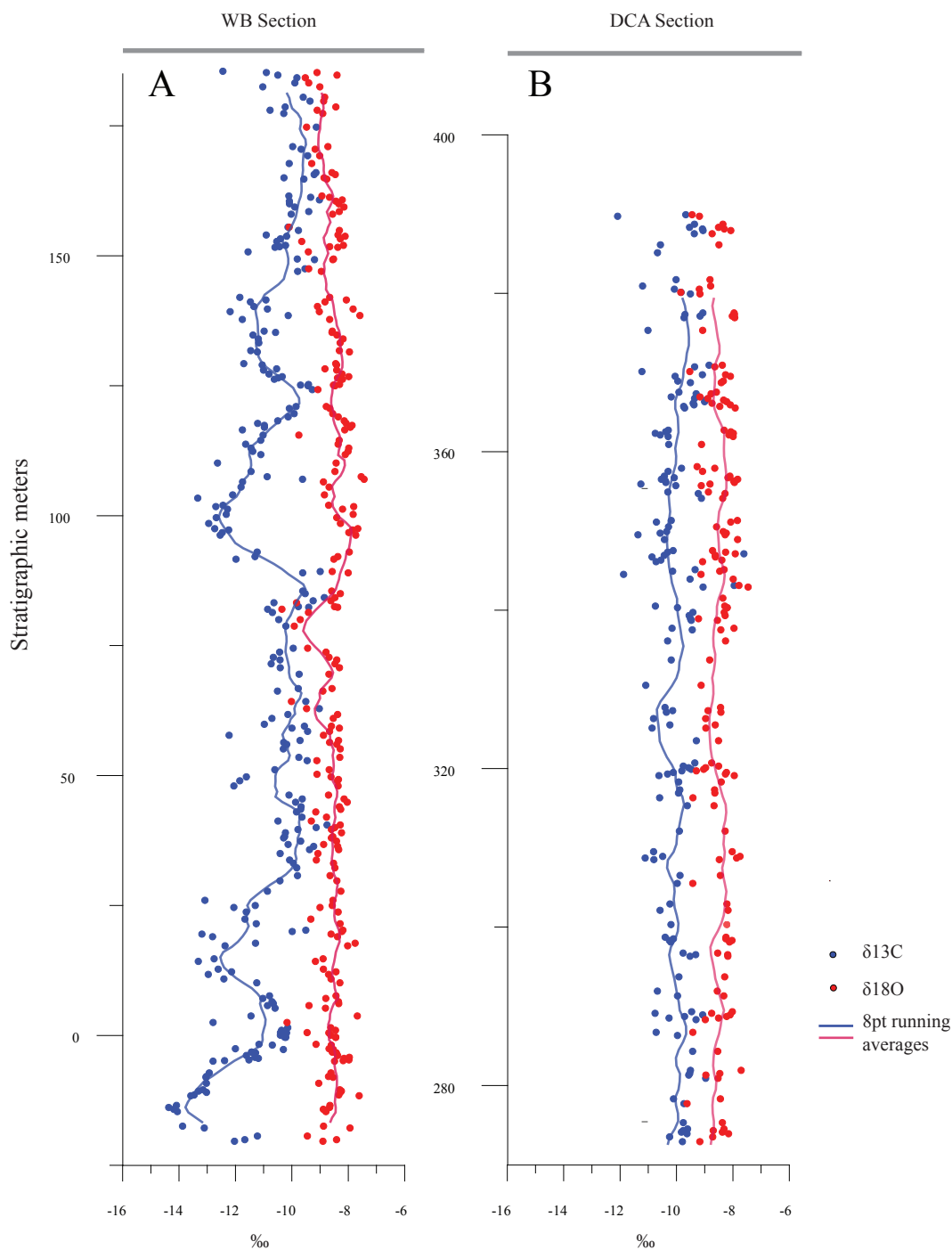


Figure 10: $\delta^{13}\text{C}$ and $\delta^{18}\text{O}$ records for the WB section (A) and DCA section (B). Red and blue lines are 8 point moving averages trough the $\delta^{13}\text{C}$ and $\delta^{18}\text{O}$ records.

against stratigraphic level. The average standard deviation for the difference between nodules at one level of $\delta^{13}\text{C}$ was 0.33‰ (n = 81). The standard deviation for the IAEA CO-1 standard is 0.14‰ ($\delta^{13}\text{C}$) and 0.09‰ ($\delta^{18}\text{O}$) for the DCA section measurements and 0.10‰ ($\delta^{13}\text{C}$) and 0.09‰ ($\delta^{18}\text{O}$) for the WB section measurements.

Other isotope measurements studies from the Bighorn Basin (Abels et al., 2012 and van Yperen, 2012), show that the standard deviation for nodules within one stratigraphic level is ~0.2‰. Therefore, we excluded measurements that distinctly, more than 2‰, fell from the trend.

Rarely both sections contain iron-oxide nodules, isotopes values do not seem to be affected by the different contents of these nodules. Not many of these nodules (10) were retrieved and only five could be measured.

Carbonate nodules should be sampled from 30 cm below the topsoil to avoid mixing with atmospheric CO_2 since atmospheric carbon has higher $\delta^{13}\text{C}$ values (Koch et al., 1992). However, we were not able to pinpoint the topsoil in some cases and sampled all nodules present. In the first 25 m of the WB section the paleosols have been pointed out more precise, allowing us to test if sampling levels 30 cm from the top of paleosols affects the $\delta^{13}\text{C}$ value of nodules substantially. Nodules that were sampled at 30 cm from the top of a paleosol are listed in bold in Appendix 2. Two of the nine samples give substantially higher values; this might be due to the influence of atmospheric CO_2 . A remark has to be made that both samples are derived from relatively incipient soils with 50% sandstones. Those paleosols could as well be interpreted as a thicker soil with sandstone levels in between since sand is deposited very rapidly.

Diagenetic spar is occasionally present in carbonate nodules and has $\delta^{13}\text{C}$ values around 11.5‰ with oxygen isotopes values much lower than micritic carbonate. Bowen et al. (2001) explained the lower oxygen isotope values by the $\delta^{18}\text{O}$ precipitation relation to temperature, a 2°C increase in temperature results in a 1‰ decrease in $\delta^{18}\text{O}$. The higher temperature is than due to burial of the soil after which nodule formation took place.

4.5.1. The isotope record of the WB section

The carbon isotope data measured from the WB section reveals four major negative $\delta^{13}\text{C}$ excursions of -3.8‰, -2.9‰, -2.7‰ and -1.8‰ (Figure 10a). Determining the value of an excursion is not straightforward. To minimize relative differences between excursions, we chose the following method: The value of an excursion is defined by the average of the $\delta^{13}\text{C}$ values that lie within the lowest 30% of the difference between the base level and lowest data point. The base level is somewhat arbitrary defined as the mean $\delta^{13}\text{C}$ value between 151.625 and 174.75 meter. The base level then has a mean $\delta^{13}\text{C}$ value of -9.9‰, with a standard deviation of 0.5‰. This interval is chosen as base level because it furthest away from the highest excursions and shows the least amount of outliers.

The $\delta^{18}\text{O}$ values do not show clear patterns, but during the two last two CIE's the $\delta^{18}\text{O}$ seem to minorly mirror the excursions (Figure 10a) and show somewhat higher $\delta^{18}\text{O}$ values. One more prominent $\delta^{18}\text{O}$ peak is present from meter 73 to 82.

4.5.2. The isotope record of the DCA section

The isotope record of the DCA section is plotted in respect to the WB section, such that the top of the WB sections is 0 m. In comparison to the WB section the isotopes in the DCA section show a fairly straightforward fingerprint, most samples fall around a value of -10 ‰ for the $\delta^{13}\text{C}$ and -8.5 for the $\delta^{18}\text{O}$.

4.5.3. Composite carbon isotope record - "Deer Creek composite"

Combining the carbon isotope data of the previous studied CSH and UDC sections with the presented WB and DCA sections spans a total record of 389.92 m we label "Deer Creek composite" (Figure 11). The different isotope records are tied together using the distinctive purple layers. The four CIE's are evident and the first two excursions scale alike in all three sections that encompass the excursions.

This long record spanning several carbon excursions allows us to test for longer scale cyclicity. Spectral analysis of the Blackman-Tuckey method applied with a 90% certainty interval and a Bartlett window shows one peak in the longer cyclicity range (22-55 m) that is not conclusive (Figure 12a). Therefore, the Blackman-Tuckey window was applied at a 90% certainty interval, resulting in a significant peak of 22-55 m (Figure 12b). The Redfit method with a 99% chi cutoff clearly shows one broad significant peak from 27 to 32 m.

The 22-55 m power spectra result from the Blackman-Tuckey method gives the widest power spectrum of long-scale cyclicity and is therefore used to limit the bandpass filter. The 22-55 meter filter neatly follows the carbon isotope excursions and filters two cycles between the two sets of isotope excursions (Figure 11). Two more cycles could be interpreted before the carbon isotope excursions; below meter 270 the signal becomes enigmatic.

4.6. Cyclostratigraphic integration

An integration of the lithological and cyclostratigraphical data is performed in Figure 13. The most apparent feature is the relation between the excursions in the carbon isotope data and the avulsion/overbank cycles that have been indicated as distinct (indicated in red). Whenever the isotope excursions are maximal, around meter 12, 100 and 135, prolific overbank/avulsion cycles are present (indicated in red). Additionally, the absence of the distinct purple layers corresponds with the lack of carbon excursions.

The bandpass filter of the redness correlates with an inverse proportional relation to the isotope excursions. It has the largest amplitudes between the first isotope excursions and between the last isotope excursions. The smallest amplitudes concur with the carbon excursion maximums. For the isotope excursion at ~ 100 m this does not hold, the redness filter is blurred by overbank/avulsion cycle M that is hard to distinguish in terms of soil development.

Figure 11 (page 21, upper figure): "Deer Creek Composite" carbon isotope record. Carbon isotope data from the WB, CSH, DCA and UDC sections. WB and DCA sections are measured in this study while the CSH record is from van Yperen, 2012 and the UDC section from Abels et al., 2012. WB, CSH and UDC sections are tied on the basis of 7 distinct purple layers. Red line is the 22-55 m bandpass filter.

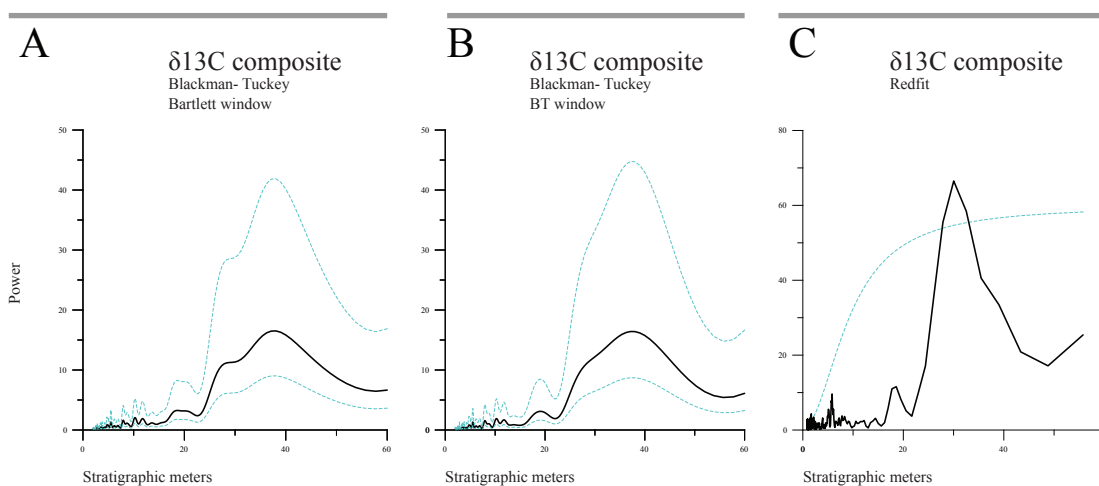
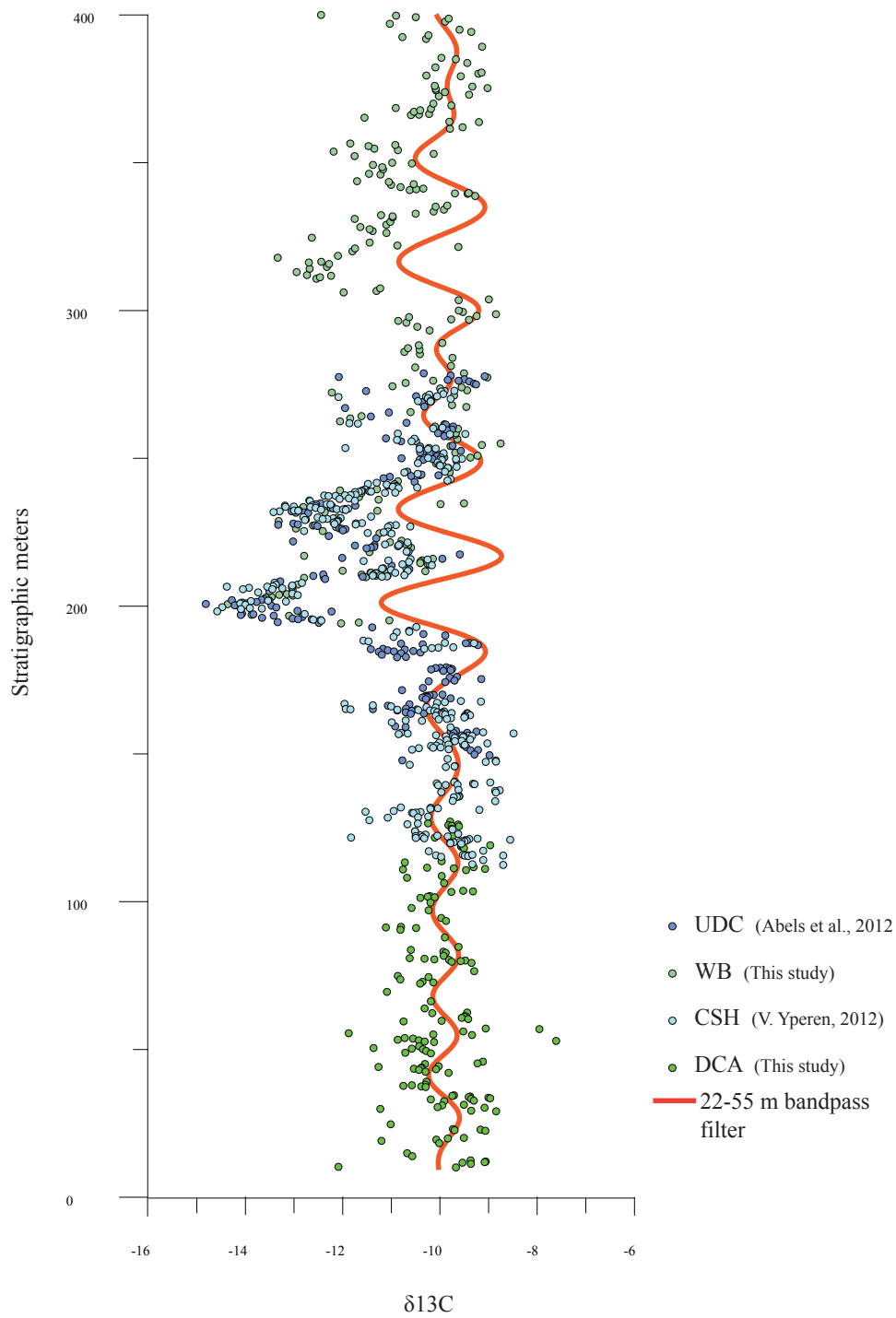


Figure 12: Blackman-Tukey and Redfit spectra for the combined isotope data, the Deer Creek Composite. For the Blackman-Tukey plot, the blue lines are the 90% certainty interval significance spectra. For the Redfit plot, the blue line is the 99% chi significance cut off.

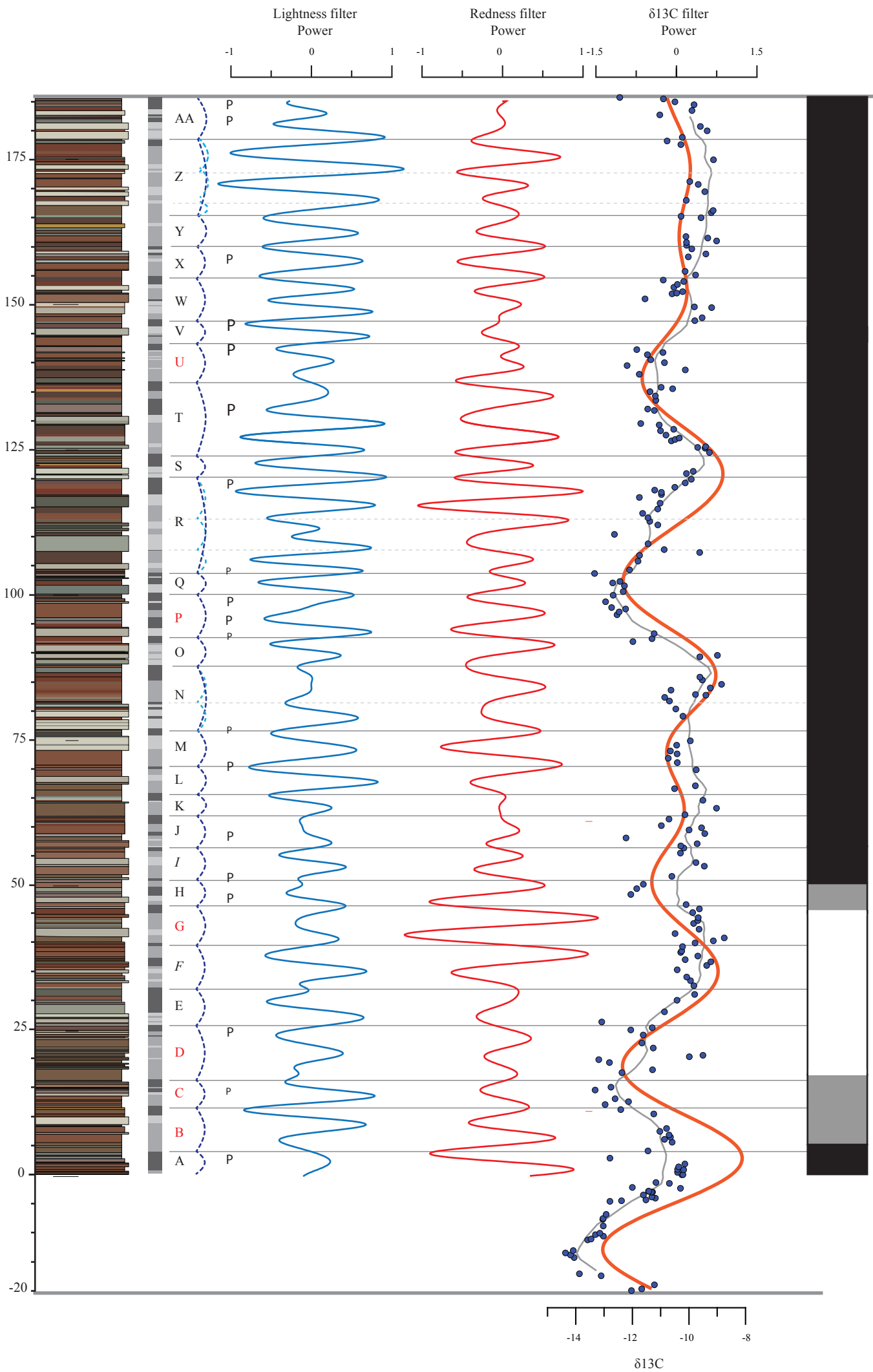


Figure 13 (page 22): Summary of the acquired color and carbon isotope data for the WB section. From left to right in the figure: the overbank/avulsion cycles, lightness filter (3.7- 10 m), redness filter (3,7- 10 m), $\delta^{13}\text{C}$ data with 8 point running average, $\delta^{13}\text{C}$ filter (22-55 m, from the Deer Creek Composite section) and the polarity pattern. Clear purple paleosols are indicated with a P (the more pronounced soil, the bigger the P).

5. Discussion

Initial age constraints for the WB section can be established on the basis of the H hyperthermals and the C24r/C24n reversal boundary from Abels et al., (2013). From these initial age constraints we derive the stratigraphic framework for the WB section and the Deer Creek composite section. The cyclostratigraphic framework of the WB section is used to extend the existing age model to the stratigraphic part of the WB section that is not covered by the section from Abels et al., (2012).

5.1. Orbital climate forcing in the WB section

5.1.1. Precessional forcing

Precession orbital forcing in the lithological record of the WB section implies that orbital forcing has an influence on the river dynamics, which are in principal controlled by autogenic processes (e.g. Abels et al., 2013). Recent literature denotes allogenic forcing as a control on the avulsion of channels in the Bighorn Basin (Abdul Aziz et al., 2008; van Yperen, 2012; Abels et al., 2013). Allogenic forcing is recognized in the lithology of the Willwood formation from color records and in the classification of sediments in overbank/avulsion cycles (Abdul Aziz et al., 2008; Abels et al., 2013). These studies claim that the overbank/avulsion cyclicity is linked to precessional orbital forcing on the basis of power spectral analysis, cycle counting, and sedimentation rates.

Magnetochron 24r studied in the Bighorn Basin by Clyde et al. (1994) has a thickness of 1219 m and an astronomical duration of 3.118 myr (Westerhold et al., 2007), corresponding to a sedimentation rate of 391 m/myr if we assume a constant sedimentation rate. The mean overbank/avulsion cyclicity of 6.4 or 7.0 m would have a duration of 16.37 or 17.90 kyr when applying the 391 m/myr sedimentation rate. A 265 m thick mammalian biochron zone, Wasachian 4, is found in the Bighorn basin (Gingerich, 2010) and indicates a comparable sedimentation rate. The duration of the biochron is 0.8 myr based on the chron 24r duration, resulting in sedimentation rates of 331 m/myr. Corresponding to this sedimentation rate the overbank/avulsion cycles would contain 19.32 kyr and 21.13 kyr for 6.4 and 7.0 m mean cycle thicknesses respectively. Expected duration of precession cyclicity periods are between 18.8 and 22.6 kyr (Berger et al., 1992). The durations of mean cycle thicknesses results on the basis of the magnetochron are relatively low, while the biochron based ages fall within the expected precession cycle period.

The Redfit spectral analysis from the color records shows one peak of 7.1 m that is similar to the 7.0 m mean cycle thickness for the overbank/avulsion cyclicity and thus could be precession related. This peak is also incorporated in the broad significant power spectrum in the Blackmann-Tuckey analysis of the color records. The significant peaks of 3.6 and 5.4 m give much lower durations and do not correspond to precession period cyclicity

on the basis of the magnetochron and biochron.

The calculated sedimentation rates should be regarded as approximations because this method assumes constant sedimentation rates for very long periods and from events stratigraphically not exactly corresponding with our section.

In the WB section the bandpass filter derived from the redness shows 34 cycles. With one precession cycle per 17.9 kyr or 21.1 kyr the section spans a minimum of 670 kyr, and a maximum of 717 kyr (based on the overbank/avulsion cycle thickness of the WB section). The lightness shows an extra cycle, appointing the section a duration of 690 to 739 kyr. A total of 6 complete and 1 incomplete 100 kyr cycles can be interpreted, despite that after the CIE at ~ 135 m the short term eccentricity signal becomes hard to distinguish. This results in a total duration of ~ 660 -690 kyr for the section. This concurs with the duration of the section from the amount of precession cycles from the redness bandpass filter.

The short and long term eccentricity is described to alter the precession amplitude (Berger, 1978). Three to four clear precession cycles should alternate with one or two indistinct precession cycles. During eccentricity maxima the precession cycles have maximum amplitude resulting in the largest differences of orbital forcing on climate and therefore, the effect on sedimentation. Hence, we would expect to see changes in the amplitude of color records and overbank/avulsion cyclicity, resembling the relation between the precession and eccentricity signal. The redness filter has an inverse proportional correlation with the carbon excursions. This correlation is as well shown with the H1 and H2 excursions in the CSH section (van Yperen, 2012). Comparing the lightness filter with carbon isotope excursions does not result in any correlation. Moreover, a clear 4 or 3:1 ratio between clear paleosols and less developed paleosols is not seen in our section.

However, the study by Van Yperen (2012) showed that 1D sections from the Willwood Formation can be very deceiving. The substantial lateral differences in overbank/avulsion cycle thicknesses and paleosol development cause us to be very conservative of basing hypotheses on our 1D lithological column. The lack of the 4-3:1 paleosol development ratio and the differences in cycles from the bandpass filters and overbank/avulsion cycles as interpreted from the lithology can easily be a derivative from the use of a 1D section.

5.1.2. Eccentricity orbital forcing

The H hyperthermals from the marine realm are described to be eccentricity related (Cramer et al., 2003). Since the carbon isotope 22-55 m bandpass filter follows the H hyperthermals, we suggest that this bandpass filter reflects the short term eccentricity orbital forcing. The influence of eccentricity in the WB section is supported by the relation between the bandpass filter and lithology. The well developed overbank/avulsion cycles are related to the excursions in the bandpass filter (Figure 13), implying that the minima in the bandpass filter, and thus the eccentricity maxima, reflects climatological processes. Whether the correlation of well developed paleosol cycles and eccentricity maxima means that climate becomes dryer or wetter

during hyperthermals is still under debate. Kraus and Riggins (2007) described a drying in the Bighorn Basin during the PETM while others suggested that the Mean Annual Precipitation was higher during the H hyperthermals in the Bighorn Basin (Bowen et al., 2004; Wing et al., 2005; Van Yperen, 2012). The short eccentricity curve itself is directly influenced by the longer (405 kyr) eccentricity (Berger, 1978). Therefore, a bundling of short term eccentricity is expected with a maximum each 4 cycles. The CIE maxima at H1-H2 and at 100 and 135 meter suggest those are both 405 kyr eccentricity maxima. This implies a long term eccentricity minimum in the interval between 45 and 85 meter.

5.1.3. I1 and I2 hyperthermals in the WB section

We know from the marine realm that the I1 and I2 hyperthermals are present in the 400 kyr eccentricity maximum after the H hyperthermals (Cramer et al., 2003). Therefore, we conclude that the two CIE's at ~100 and ~135 m are the continental equivalent of the marine I1 and I2 hyperthermals. 15 precession cycles are expected between the H2 and I2 hyperthermals because 3 short eccentricity cycles separate those hyperthermals. Between the H2 and I1 hyperthermals the redness filter shows 14 cycles with a possible four extra cycles (within alternation M), the lightness shows 17 cycles with four possible extra cycles (within overbank/cyclicality cycles J and M), and the lithology shows 13 cycles. The amount of precession cycles between H2 and I1 from the different proxies do not fit one-on-one. However, taking into account the uncertainty of the proxies the conclusion that I1 and I2 are present in the WB section is strengthened by the precession.

From the astronomical age of the hyperthermals we can calculate sedimentation rates independent of the constraints from other sections. The I hyperthermals span 37 and 33 m stratigraphically, and 100 kyr from a temporal perspective. This results in sedimentation rates of 3.0 kyr/m and 2.7 kyr/m. A precession cycle of 7.0 m thick would span 21.2 kyr or 18.9 kyr, which is in agreement of the precession range of Berger et al. (1992).

5.2. Comparison of the WB section and hyperthermal magnitudes therein to the marine realm

Now we have established the cyclostratigraphy framework for the WB section, a comparison can be made to the marine realm. The cyclostratigraphy for the H1 to I2 interval of Westerhold et al. (2012) based on ODP Sites 1258 and 1262 is a marine counterpart of the WB section. The eccentricity is constrained on the basis of $\delta^{13}\text{C}$ records while the precession proxy are Fe intensity records. The correlation is made on the basis that $\delta^{13}\text{C}$ values are the same in oceans and atmosphere on a geological time scale (> 1 kyr) (McCarren et al., 2008).

5.2.1. Comparison of the WB section to the marine realm

The correlation between the marine section of Westerhold et al. (2012) and our study is presented in Figure 14. The similarity between the short eccentricity filters (orange lines) is striking; both filters show larger amplitudes for the H and I hyperthermals. As well, two filtered cycles are present between H1 and H2 hyperthermal.

Westerhold et al. (2012) shows 23.5 precession cycles between the onset of H1 and the offset of I2. The overbank/avulsion pattern show 22 precession cycles when overbank/

avulsion cycle R contains 3 cycles. In the WB section the lightness filter gives 27 cycles whereas the redness displays 24 cycles. The redness coincides almost one-on-one with the precessional signal from the Fe records. From the onset to the offset of the hyperthermals (H2-I2) the marine record shows 3.5 precession cycles per hyperthermal, only in the H2 event the redness does not match perfectly and misses half a cycle (brown and blue shadings).

The correlation to the marine realm confirms the suggestion that the short eccentricity cycles are indeed present in the carbonate isotope record of the WB section. The hyperthermals I1 and I2 in both realms are one short eccentricity cycle apart. Both I hyperthermals include five precession cycles from the lowest point on both sides of the peak in the filter from Westerhold et al. (2012) (Figure 15). In the WB section these hyperthermals span ~5.5 precession cycles in the redness bandpass filter.

The precessional signal from the color records and the overbank/avulsion cyclicity is not unequivocal as discussed earlier, for that reason a comparison for the precessional signal between the WB section and the marine realm is hampered. However, a very good correlation between the redness and the marine Fe-records could be established, which strengthens our conclusion that the cyclicity in the WB section is orbitally forced.

5.2.2. Magnitudes differences between marine and continental hyperthermals

Attempts by Bowen et al. (2004) to address the amplified continental $\delta^{13}\text{C}$ records in respect to the marine records provided three possible explanations. The first is the temperature effect on carbon isotope fractionation between CO_2 gas, dissolved inorganic carbon and CaCO_3 in the ocean surface water and soils. The second option related to changes in the surface ocean carbonate ion concentration. Changes in soil productivity and organic matter turnover rates provide the last option. The main reason of $\delta^{13}\text{C}$ magnitude amplification of plants in carbon models was found to be the influence of humidity (Bowen et al., 2004). Humidity influences the $p\text{CO}_2$ which in turn controls the uptake of depleted carbon. As a result, these authors concluded that a change to a more humid climate explains the terrestrial CIE amplification. However, Bowen et al. (2004) presumed linear relations between the $p\text{CO}_2$ and $\delta^{13}\text{C}$ discrimination.

Having established the presence of the I1 and I2 hyperthermal in the WB section, we extend the comparison between the continental and marine CIE's from Abels et al. (2012). These authors show a linear trend for the comparison between marine and continental H and PETM excursions. This linear trend suggests that all hyperthermals are the results of the same process of processes. However, as they state in the paper, the linear scaling does not yield the origin of the graph. This leads to a 2‰ CIE in the continental realm when there is no CIE in the marine realm. This offset can either be explained by an unknown mechanism affecting $\delta^{13}\text{C}$ at lower values, or by a nonlinear relation between the uptake of $\delta^{13}\text{C}$ and the atmospheric $\delta^{13}\text{C}$ values in one of the realms

Comparing the hyperthermals including I1 and I2 reveals a trend that can be explained by an exponential relation between continental and marine records (Figure 15a, Box 1). Two alternative options are a linear scaling from the PETM to I1 with I2 as an outlier or a linear scaling from H1 to I2 with the PETM as deviating hyperthermal. The correlation between the marine hyperthermals from different sites and records inhibit a linear

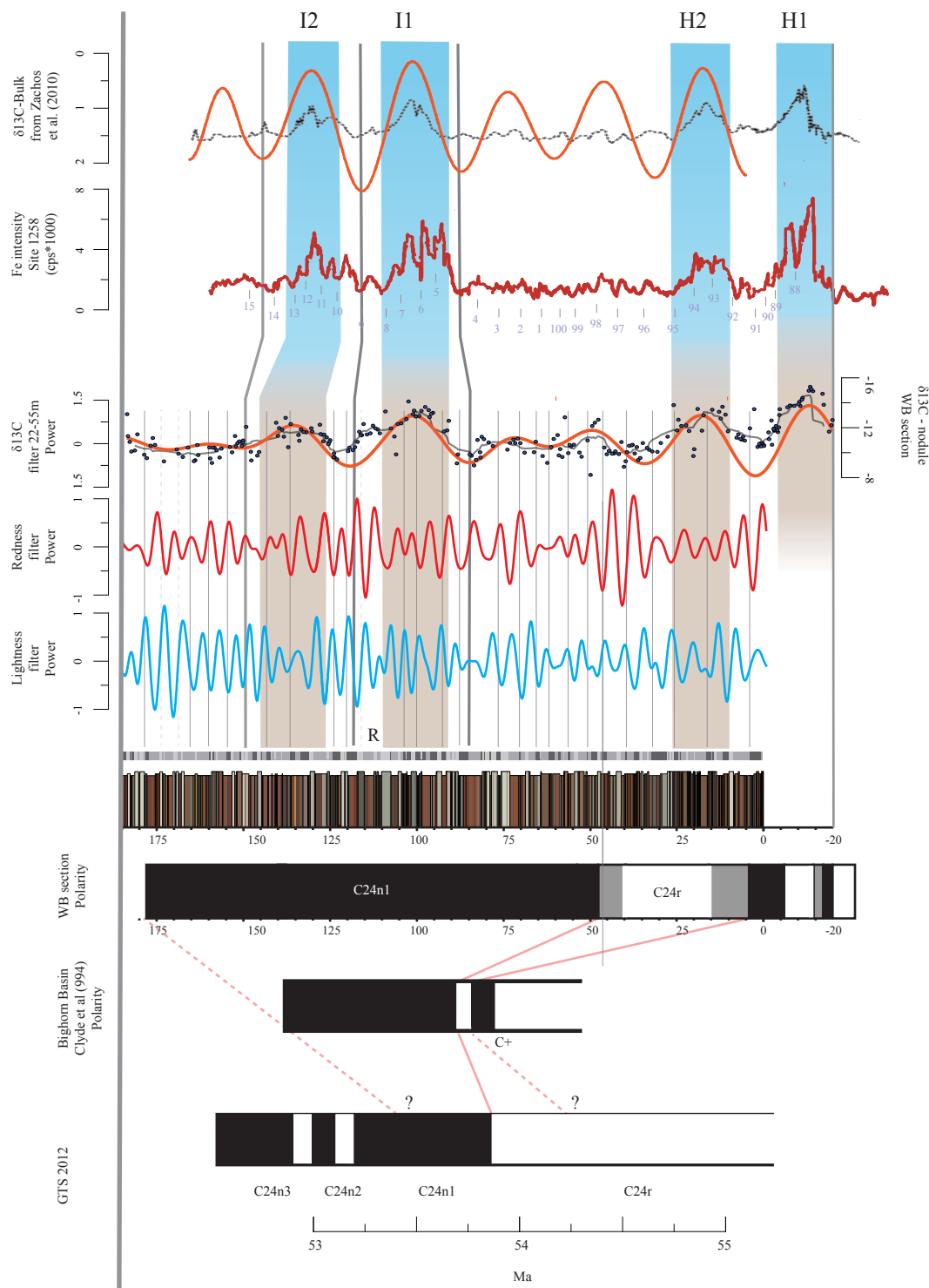


Figure 14: Comparison of the WB section to Westerhold et al. (2012). In the part above (blue part), orange is the short eccentricity filter. Red, Fe intensity data of ODP site 1258. In black, the $\delta^{13}\text{C}$ of the bulk carbonate (ODP site 1262). The middle part (brown) is the WB and Deer Creek composite data. In the lower part the correlation to the GTS2012 is plotted.

relationship (Figure 15b). The differences in the absolute values of $\delta^{13}\text{C}$ records between different sections in the marine realm can be attributed to differences in productivity and terrestrial input (McInerney and Wing, 2011, and references therein). Since the oceanic bulk and foraminiferal carbon responded with a linear carbon intake to the higher carbon levels in the atmosphere, the cause of the exponential relationship has to be sought in the way nodules record $\delta^{13}\text{C}$.

A different process of nodule carbon fractionation at high or low pCO_2 is needed if the PETM and I2 are real outliers from a linear trend. At the moment no process that would explain this fractionation behavior is known. Another option is that the hyperthermal magnitude is wrong. Since the background value

in the WB section and marine sections is quite clear and the I1 hyperthermal uses the same value this will not be the case for the I2 hyperthermal. However, the continental and marine $\delta^{13}\text{C}$ records show different onsets for the PETM. The offset in the continental realm is more gradual and ends later than in the marine records. For our correlation we took the background values before the PETM, there the values are the least influenced by the hyperthermal. If the background value is taken closer to the marine offset the magnitude of the continental PETM value is lowered and will fall on the linear trend from I1 to H2. But because the continental PETM $\delta^{13}\text{C}$ record reaches the same levels before and after the PETM we argue that the $\delta^{13}\text{C}$ levels before the PETM represent the background $\delta^{13}\text{C}$ value.

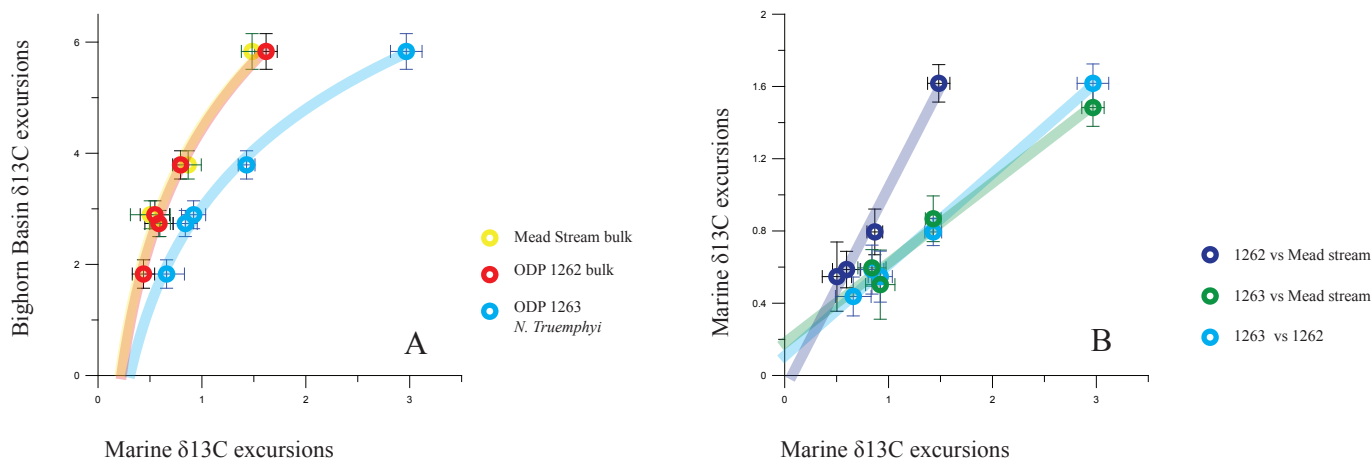


Figure 15: CIE comparison of the marine and continental Bighorn Basin (BH) records (**A**). Yellow: BH versus bulk carbonate of the Mead Stream (Slotnick et al. 2011). Red: BH versus Walvis Ridge ODP 1262 bulk carbonate (Zachos et al 2010, H1 is taken from ODP 1267 because of severe carbonate dissolution in core 1262). Blue: BH versus ODP site 1263 (N. Truempyi), PETM, H1 and H2 are from Stap et al. (2009;2010). I1 and I2 from Laurentano (Pers. communication). **B:** CIE comparison of records from the marine realm, the same data is used as in Figure 15A. Purple: ODP 1292 versus Mead Stream. Green: ODP 1263 versus Mead Stream. Blue: ODP 1263 versus 1262. Mean Difference (MD) is indicated by lines stretching out from the data points.

We conclude that an exponential relation is the most probably relation between the marine and continental hyperthermals.

The exponential relation between the marine and continental $\delta^{13}\text{C}$ records is in contrast to the linear relation found by Abels et al. (2012). The exponential trend lines do not intercept the origin either, our findings result in a minor $\sim 0.25\%$ $\delta^{13}\text{C}$ excess for the marine realm. The reason for the offset to the origin might be an overestimation of the marine hyperthermals in respect with the continental hyperthermals, an underestimation of the continental hyperthermals with respect to the marine hyperthermals or a physical process that is yet unknown. Abels et al. (2012) conclude that the hyperthermals have a similar origin which is confirmed by the exponential function that fits all hyperthermal magnitude comparisons.

A possible explanation for the exponential relation described here, is provided by a recent study that studied the effects of rising pCO_2 on the $\delta^{13}\text{C}$ discrimination by plants that resemble the flora of the Early Eocene. This study shows that plants act as a filter which discriminates between the pCO_2 and the uptake of $\delta^{13}\text{C}$ with a hyperbolic relation (Schubert and Jahren, 2012). These results could explain the results as we show in here because the hyperbolic and exponential equations are similar before reaching asymptotes. Both equations show that during lower $\delta^{13}\text{C}$, or pCO_2 values, the $\delta^{13}\text{C}$ discrimination in plants is higher than during high $\delta^{13}\text{C}$ conditions. With the new data provided by this study a more accurate carbon model could be established on the basis of an exponential relation between terrestrial and marine CIE's. Ultimately the actual $\delta^{13}\text{C}$ value could be resolved which would lead to a better estimate for the amount of Gt carbon injected in the atmosphere during hyperthermals.

5.2.3. Origin of the depleted $\delta^{13}\text{C}$

The provenance of the depleted carbon that was injected in the atmosphere is still under debate. Our results show that all hypothesis that explain different causes between hyperthermals can be excluded. Furthermore, a plausible explanation for the cause of carbon injection should follow the astronomical forcing (Lourens et al., 2005; Stap et al., 2009; Westerhold et al., 2012). A comet impact or oxidation of organic carbon in seaways resulting from tectonic uplift would have an impact

on the carbon cycle, but not on a temporal scale that matches the orbital forcing (Kent et al, 2003; Higgins and Schrag, 2006). Another option entails an output of magmatic fluid in the North Atlantic at the time of the PETM. Subsequent hyperthermals are then driven by the orbital forcing controlled carbon cycle feedback (Westerhold et al. 2011). Sexton et al., (2011) describes the redistribution of carbon due to strengthened oxidation of dissolved oceanic organic carbon to account for an influx of carbon in the atmosphere. The initial warming causing the redistribution of carbon is again induced by orbital forcing. This theory would require a secondary carbon source to explain the PETM CIE magnitude. In both options, the PETM must have been fueled by an extra sedimentological source in respect to the other hyperthermals. These options do not correspond to our conclusion that all hyperthermals are driven by the same process or processes.

The burning of peat is a sedimentological source of depleted $\delta^{13}\text{C}$ (Kurtz et al, 2003), but according to Dickens (2011), the peat reservoir would be too small to account for the $\delta^{13}\text{C}$ magnitudes. Due to the lack of glaciation on Antarctica the thawing of permafrost could as well explain the release of carbon (DeConto et al., 2012). According to this hypothesis, permafrost was initially warmed by higher solar insolation from orbital forcing; the carbon stored in the permafrost then provided carbon causing the hyperthermals. This recent hypothesis is not matured and needs further proof in terms of geological data.

The most accepted option appears to be the thermal discharge of gas hydrates (CH_4) that oxidizes to CO_2 when released to the ocean or atmosphere (Dickens and O'Neil, 1995; Dickens, 2011). Gas hydrates form on continental slopes when the temperature is relatively low. Therefore, their stability depends heavily on the seafloor temperature (Dickens, 2001b). Although the gas hydrate dissociation hypothesis is promising, it is far from established. No positive evidence is available for the hypothesis since essential knowledge is lacking, such as the amount of gas hydrates at present times (Dickens, 2011). The gas hydrates alone are not sufficient to account for the cause of the hyperthermals. An initial temperature increase from orbital forcing at the seafloor is needed to overcome the temperature threshold at which the carbon bearing hydrates start to melt and are released to the ocean and atmosphere.

Box 1

Determining the value of the CIE's.

Assessing a value for a CIE depends on two choices, what is the $\delta^{13}\text{C}$ baselevel and what is the CIE maxima. The baselevel has to be chosen before the hyperthermal to filter out recovery influences of the hyperthermal and to be the mean of several data points. In the case of H1-I2 the base has been chosen before H1 to prevent earlier hyperthermals to from altering later hyperthermal CIE values. In this way we assume a constant baselevel throughout H1-I2. For the PETM in marine sections the baselevel can be hard to establish because carbon dissolution occurred before the PETM.

The maximum of a CIE is defined as the mean of the $\delta^{13}\text{C}$ values that fall within the lowest 30% of the distance between baselevel and the absolute lowest $\delta^{13}\text{C}$ value measured. The 30% was chosen to correspond to the Bighorn Basin PETM value from Abels et al. (2012) and fits very nicely with the H1 and H2 from these authors. The mean difference, or the error bar, is calculated as

$$MD = \sqrt{\sigma_{\text{hyperthermal}} / n_{\text{hyperthermal}} + \sigma_{\text{baseline}} / n_{\text{baseline}}}$$

5.3. Magnetostratigraphic correlation to the Geological Time Scale 2012

The UDC section records the C24r/C24n reversal boundary (Abels et al., 2012). Therefore, we conclude that the main reversal at 47 m in the WB section concurs with the C24r/C24n reversal (Lower part Figure 15). The reversal by Abels et al. (2012) has an uncertainty range of ~58 m, while our study establishes the reversal with an uncertainty of ~7 m. The short normal polarities changes within C24r in the WB section could be interpreted as short period intensity variations of the dipole field termed cryptochrons (Cande & Kent, 1992), or might be a result of sample handling. A third explanation is a very short field variation that is not recorded in marine records, but can be recorded in continental sections.

In the WB section the upper thin polarity interval is situated stratigraphically at a maximum ~ 45 m below the C24r/C24n reversal. With the sedimentation rate derived from the astronomical duration of the I hyperthermals this results in an ~136.4 kyr or ~121.6 kyr interval between the C24r/C24n reversal boundary and the upper thin polarity interval. The lower thin polarity change is situated ~65 m below the C24r/C24n reversal boundary and is thus, ~175.7 kyr or ~196.7 kyr older than the C24r/C24n boundary. Using the same method, the upper normal polarity interval measures a minimum of 10.4 m corresponding to a minimum ~28.3 kyr to ~19.7 kyr duration. All reported cryptochrons in C24r from Cande and Kent (1992) have a duration of 9 or 10 kyr, and the first cryptochron from the C24r/C24n boundary is ~212 kyr older than the C24r/C24n reversal. However, the claim that all cryptochrons have the same duration is likely to be an artifact of the used resolution. All known chrons have different durations and no recurrent properties are involved. Therefore, it is highly contestable that all cryptochrons have the same duration. A comparison of the duration of the cryptochrons and thin polarity changes is as such, not possible.

Especially the upper thin normal polarity interval recorded in the WB section does probably not correspond to the cryptochrons found by Cande & Kent (1992), because it is found relatively short before the C24r/C24n reversal. The lower thin normal polarity interval might still be related to the cryptochron closest to the C24r/C24n reversal boundary. Although the lower thin normal polarity is 15 kyr too close to the C24r/C24n reversal boundary, we cautiously bring forward that the resolution of the study by Cande and Kent (1992) might be the cause of this offset. However, it would be very unlikely that both thin polarity changes have different backgrounds.

5.3.1. The C24r/C24n reversal boundary in the Bighorn Basin

Early Eocene magnetostratigraphic results from the Bighorn Basin show a clear polarity that corresponds with the main body of C24n. In three of the four sections containing the C24r/C24n boundary a short polarity change is recorded preceding the main reversal (Clyde et al., 2007). For example, a short normal polarity from the McCullough peak section in Clyde et al. (1994) is reported ~25 m below the main polarity change (lower part of Figure 15). A supposedly even thinner reversal like our first thin polarity change could easily be missed in records that have a lower resolution than the WB section. A polarity change in a low resolution study from the Bighorn Basin by Tauxe et al. (1994) is indeed correlated to the 24r.6 cryptochron from Cande & Kent (1992). Thus, existing literature provide evidence for short reversal patterns within the magnetostratigraphy from the Bighorn Basin.

5.3.2. Comparison to the marine magnetostratigraphic records

In the marine record Cramer et al. (2003) found the C24r/C24n reversal at different positions in respect with the H hyperthermals. In ODP 1051A and DSDP 577 the boundary could be placed somewhere below H1 or below H2. In ODP core 1051B the boundary is found from H2 to in between H2 and I1, in ODP site 550 it is situated just after H2. Our position of the reversal, in the subsequent short eccentricity maximum after H2, compares to C24n/C24r boundary in the DSDP 550 site. This position also concurs with the reversal in ODP 1258, although no carbon isotope data is shown with the reversal (Westerhold and Röhl, 2009). A marine section from Italy marks the reversal boundary just after H2 (Galeotti et al., 2010).

The WB section short normal polarity intervals correlate to the maximum of H1 and in the minimum between H1 and H2. These positions are the same as the C24r/C24n boundary in ODP site 1051A and DSDP 577. The normal polarities found earlier than H2 in the ODP cores may reflect the short polarity chrons from the WBS. In this case, the thin polarity changes are mistaken for the C24r/C24n boundary. The resolution of the magnetostratigraphy of the WB section is much higher compared to the resolution of ODP core 1051A. For instance, the ODP core contains only three data points between H1 and H2, whereas our section contains 20 data points to constrain the same interval. The ODP core shows samples with a normal polarity within the C24r chron. These samples are ignored or included within the uncertainty interval but might be related to short polarity intervals.

Short polarity changes are present in the

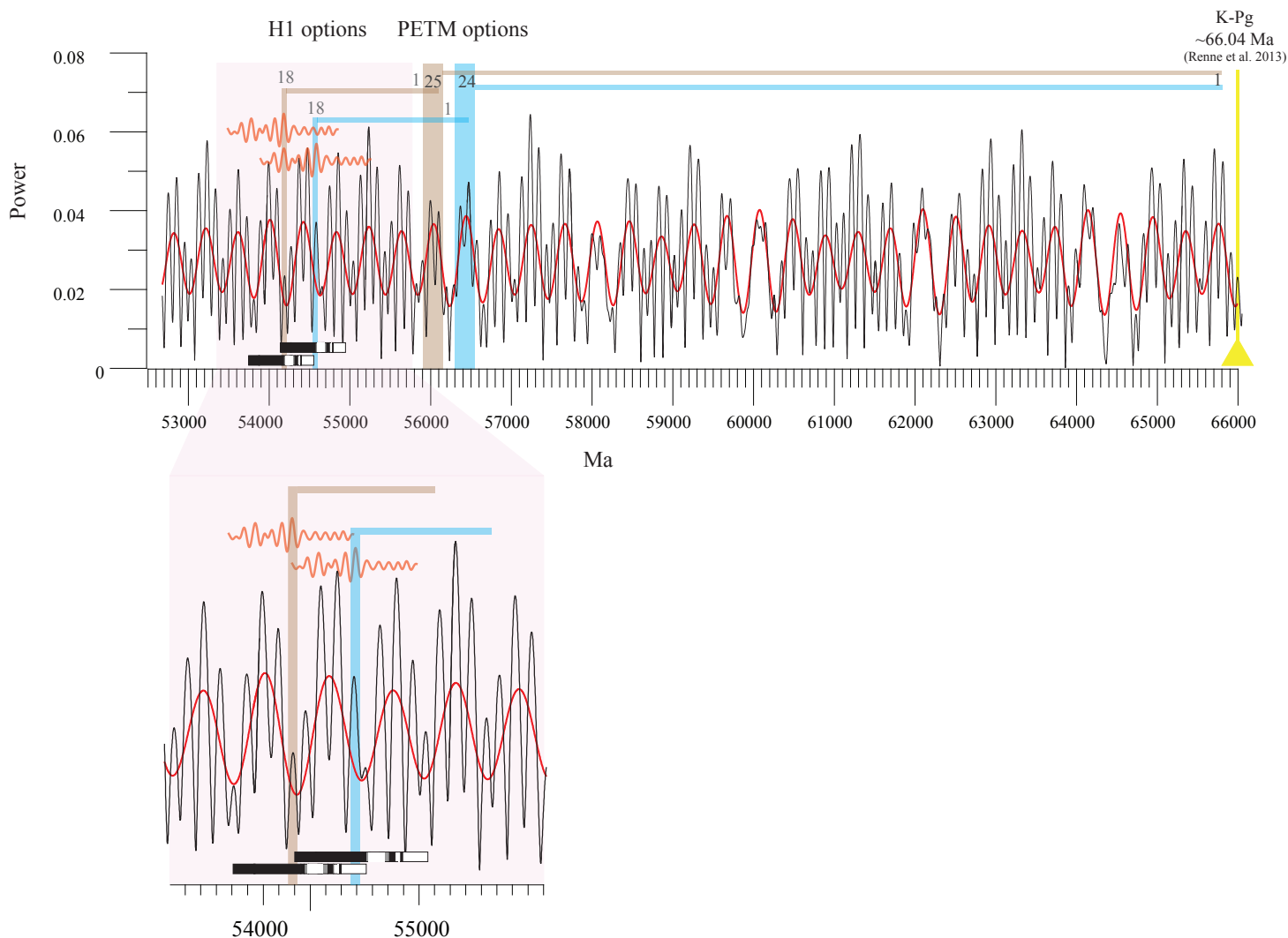


Figure 16: Tuning options for the WB section to the La2011 solution taking the K-Pg age from Renne et al., 2013. The Black line is the La2011 solution, the red line is a bandpass filter indicating the 400 kyr cyclicality. Orange lines are the 22-55 m bandpass filter derived from the Composite Deer Creek section that includes the H1-I2 hyperthermals. In the lower part the H1 options are highlighted. Note that the correlation do not include the option of 17 100 kyr cycles between the PETM and H1 since both hyperthermals would then fall within a 400 kyr minimum. However, the solution presented here correlates the H1 hyperthermal to the onset of a 400 kyr maximum, therefore, the tuning is most probably erroneous.

magnetostratigraphy of the Bighorn Basin, and looking closer to the magnetostratigraphy established in the marine realm, the ODP cores do not provide a high resolution magnetostratigraphic framework. Therefore, it seems reasonable that the short polarity patterns are real polarity changes, but are not recorded as the cryptochrons by Cande & Kent (1992). However, the magnetic signal in the WB section is far from straightforward. Other high resolution continental sections would have to be studied in order to provide a definitive conclusion regarding the short polarity intervals.

5.3.3. Dating the C24r/C24n reversal

The Neogene geological time scale has been successfully established almost entirely on astronomical forcing. A stratigraphic gap obstructs the extension of this timescale towards the Early Eocene (GTS2012). Now the C24r/C24n reversal boundary is established with an uncertainty of one precession cycle, tuning of our short eccentricity signal to the orbital solution would provide an astronomical age for the polarity reversal. To astronomically tune the Eocene or Paleocene a radiometric dating should provide the constraints

to tie a floating record to the astronomical solution.

The astronomical tuning is derived from the movement of planets that inhibit chaotic movement. The solution therefore becomes more uncertain the further the solution is calculated into the past. The 100 kyr term cannot be used further than 60 Ma (Laskar et al., 2011). It is still unclear if the 100 kyr term is reliable for the 50-54 Ma time frame (H. Abels, personal communication).

Constraining astronomical tuned ages for the Eocene and Paleocene has proved to be a stubborn point of discussion. Two additional problems apart from the astronomical solution are important to the tuning, the first being the connection between the marine records and the astronomical solution. An obvious tie point to the astronomical solution is the K-Pg boundary because of its distinctiveness in all records. Absolute dating of the K/Pg boundary has primarily been done by $^{40}\text{Ar}/^{39}\text{Ar}$ dating. The problem with this method is however, that it relies on the Fish Canyon tuff standard that has an age of 27.79 to 28.393 Ma, a variation of 2% (Rivera et al., 2011). This causes the same variation in the K-Pg age, thus excluding a direct tuning to the 400 kyr term astronomical solution. Other methods are U/Pb dating, or the direct tuning of marine records to the

astronomical solution but both methods have not resolved in a conclusive K-Pg date.

The second problem is the cyclostratigraphy. For instance, between the K/Pg boundary and the PETM Hilgen et al. (2010) found 25×405 kyr cycles for the Paleocene while Westerhold et al. (2008) recorded 24×405 kyr cycles. In addition, the amount of cycles between the PETM and H1 is under discussion. Either 17, (Westerhold et al., 2007) or 18 (Lourens et al., 2005) short eccentricity cycles are present from the top of the PETM to the base of H1.

Three options for the K/Pg dating on the basis of direct tuning of marine Paleocene/Eocene records to the astronomical solution have been given by Westerhold et al., (2007, 2008) and Westerhold and Röhl (2009). All three options are one 400 kyr cycle apart and are 65.28, 65.68 and 66.08 Ma. When counting cycles toward H1, each of these three options results in four options for the dating of H1.

A combined $^{40}\text{Ar}/^{39}\text{Ar}$ and U/Pb dating method provide strong radiometric evidence for the timing of the K/Pg boundary at 66.043 ± 0.043 Ma (Rennes et al. 2013). This dating firmly supports the oldest option from Westerhold et al. (2008). With the constraints from Kuiper et al. (2008) the K-Kg boundary would lie at 65.8 Ma according to Renne et al. (2013). This would however, put the K-Pg boundary in an eccentricity maximum while it is known from the Zumaia section in Spain that the K/Pg boundary must lie in a 400 kyr minimum (Kuiper et al, 2008). We work out the tuning of the C24r/C24n reversal boundary for the K/Pg boundary at 66.043 Ma in Figure 16.

Figure 16 shows the options for the tuning of the C24r/C24n reversal to the La2011 astronomical solution. The possibility that 18×100 kyr cycles are present between the PETM and the H1 is shown since the 17×100 kyr options correlates both hyperthermals to a 400 kyr cycle minimum, while in the former option the H2 event corresponds to a 400 kyr maximum. No tuning option correlates both hyperthermals to short eccentricity cycles that lie within a 400 kyr maximum. This could be due to an erroneous orbital solution or the tuning is incorrect. Since it is uncertain if the 100 kyr term of the orbital solution can be used in the time frame of the WB section this is a very likely cause of the offset in the tuning. The younger K-Pg age resulting from Kuiper et al., (2008) would not affect our tuning since the 400 kyr cycles are counted from the first eccentricity maximum after the K-Pg.

6. Conclusion

Our carbon isotope record reveals four major negative $\delta^{13}\text{C}$ excursions (CIE's) of -3.8‰, -2.9‰, -2.7‰ and -1.8‰, that are linked to hyperthermals H1, H2, I1 and I2. The hyperthermals are eccentricity scale paced with a 400 kyr cycle in between H2 and I1. The lithology of the WB section shows precessional scale cyclicity as overbank/avulsion cycles, corresponding to precessional cyclicity recognized in other sections from the Bighorn Basin. The cyclostratigraphic framework of our section can be confidently linked to marine records. Plotting the $\delta^{13}\text{C}$ magnitudes of the hyperthermals and the PETM against their marine equivalents reveals an exponential relation. This relationship might be explained by an exponential relation of $\delta^{13}\text{C}$ uptake by Eocene type plants and temperature.

Having established the exponential relation between marine and continental hyperthermal magnitudes supports the idea that all hyperthermals are the result of the same process of

processes. Therefore, proposed origins for excess carbon during hyperthermals do not fulfill this criterion are highly unlikely.

Further, this relation might be the starting point for a better understanding of the carbon cycle. That eventually can lead to an estimate for the $\delta^{13}\text{C}$ magnitudes of the atmosphere during hyperthermals. In turn, this can be the basis for the development of a model that predicts how much carbon actually was released during hyperthermals.

Additionally, we established the C24r/C24n paleomagnetic boundary to be present in the maximum of one short eccentricity cycle after H2. Short polarity changes before the main reversal boundary might be the reason that in marine records the boundary is not defined homogeneously.

7. Acknowledgements

First of all I would like to thank Hemmo Abels for the opportunity to work on this project, and all his precious time and effort he put into the guidance of my thesis. Secondly, I would like to thank the others of the Bighorn Crew: Philip Gingerich for staying at his house, valuable discussions and for driving his cars. Jort Koopmans for his relentless trenching and for the use of the “master computer” at the office, among other things. Marijn Koopman is thanked for the help with the logging during her holidays. Peter van de Berg and Sander Smeets are both thanked for their contributions to the fieldwork and good atmosphere at the fieldcamp. Arnold van Dijk is thanked for the isotope measurements. I thank Frits Hilgen for many huge improvements to the manuscript and Vittoria Lauretano for the use of her data. I also want to thank everyone involved at N318 and the people who helped improving my drafts.

At last I want to thank friends and family for their support, even though they thought I was only seeking worms with a shovel.

8. References

- Abdul Aziz, H., Hilgen, F.J., Van Luijk, G.M., Sluijs, A., Kraus, M., Pares, J.M., Gingerich, P.D., 2008. Astronomical climate control on paleosol stacking patterns in the upper Paleocene–lower Eocene Willwood Formation, Bighorn Basin, Wyoming. *Geology* 36, 531.
- Abels, H.A., Clyde, W.C., Gingerich, P.D., Hilgen, F.J., Fricke, H.C., Bowen, G.J., Lourens, L.J., 2012. Terrestrial carbon isotope excursions and biotic change during Palaeogene hyperthermals. *Nature Geoscience* 5, 326–329.
- Abels, H.A., Kraus, M.J., Gingerich, P.D., 2013. Precession-scale cyclicity in the lower Eocene fluvial Willwood Formation of the Bighorn Basin, Wyoming (USA). *Sedimentology*. Accepted.
- Balsam, W.L., Deaton, B.C., Damuth, J.E., 1999. Evaluating optical lightness as a proxy for carbonate content in marine sediment cores. *Marine Geology* 161, 141–153.
- Berg, van den, F., 2012. The Willwood Formation, Wyoming, USA: Autogenic or precession controlled deposits - A combined fieldwork and modeling approach. University of Utrecht (master thesis).
- Berger, A., 1978. Long-Term Variations of daily insolation and quaternary climatic changes. *Journal of the Atmospheric Sciences*, 35, 2362–2367.
- Berger, A., Loutre M.F., and Laskar J., 1992. Stability of the astronomical frequencies over the Earth's history for paleoclimate studies. *Science*, 255, 560–566.
- Blackman, R.B., and Tukey, J.W., 1958. The measurement of power spectra from the point of view of communication engineering. Dover Publications, 190 pp.
- Bowen, G., Zachos, J.C., 2010. Rapid carbon sequestration at the termination of the Paleocene-Eocene Thermal Maximum. *Nature Geosciences* 3, 866–869.
- Bowen, G., Beerling, D., Koch, P., 2004. A humid climate state during the Palaeocene/Eocene thermal maximum. *Nature* 312, 866–869.
- Bowen, G., Koch, P., Gingerich, P., 2001. Refined isotope stratigraphy across the continental Paleocene-Eocene boundary on Polecat Bench in the northern Bighorn Basin. Paleocene-Eocene stratigraphy and biotic change in the Bighorn and Clarks Fork basins, Wyoming. University of Michigan Papers on Paleontology, 33: 73–88.
- Bown, T., Kraus, M., 1987. Integration of channel and floodplain suites, I. Developmental sequence and lateral relations of alluvial paleosols. *Journal of Sedimentary Research* 57(4), p.587–601.
- Cande, S., Kent, D., 1992. A new geomagnetic polarity time scale for the Late Cretaceous and Cenozoic. *Journal of Geophysical Research* 97, 13917.
- Clyde, W.C., Hamzi, W., Finarelli, J. a., Wing, S.L., Schankler, D., Chew, A., 2007. Basin-wide magnetostratigraphic framework for the Bighorn Basin, Wyoming. *Geological Society of America Bulletin* 119, 848–859.
- Clyde, W.C.J.S. and P.D.Gi., 1994. Chronology of the Wasatchian Land-Mammal Age (Early Eocene): Magnetostratigraphic Results from the McCullough Peaks Section, Northern Bighorn Basin, Wyoming. *Geology* 102 (4), pp. 367–377.
- Cramer, B.S., 2003. Orbital climate forcing of $\delta^{13}\text{C}$ excursions in the late Paleocene–early Eocene (chrons C24n–C25n). *Paleoceanography* 18, 1–25.
- Davis, J. C., 1986. *Statistics and Data Analysis in Geology*. John Wiley & Sons, New York.
- DeConto, R.M., Galeotti, S., Pagani, M., Tracy, D., Schaefer, K., Zhang, T., Pollard, D., Beerling, D.J., 2012. Past extreme warming events linked to massive carbon release from thawing permafrost. *Nature* 484, 87–91.
- Dickens, G., O'Neil, J., 1995. Dissociation of oceanic methane hydrate as a cause of the carbon isotope excursion at the end of the Paleocene. *Paleoceanography* 10, 965–971.
- Dickens, G.R., 2011. Down the Rabbit Hole: toward appropriate discussion of methane release from gas hydrate systems during the Paleocene-Eocene thermal maximum and other past hyperthermal events. *Climate of the Past* 7, 831–846.
- Diehl, J.F., Beck, M.E., Beske-Diehl, S., Jacobson, D., Hearn, B.C., 1983. Paleomagnetism of the Late Cretaceous-Early Tertiary north-central Montana Alkalic Province. *Journal of Geophysical Research* 88, 10593.
- Friend, P.F., Slater, M.J., Williams, R.C., 1979. Vertical and lateral building of river sandstone bodies, Ebro Basin, Spain. *Journal of the Geological Society* 136, 39–46.
- Galeotti, S., Krishnan, S., Pagani, M., Lanci, L., Gaudio, A., Zachos, J.C., Monechi, S., Morelli, G., Lourens, L., 2010. Orbital chronology of Early Eocene hyperthermals from the Contessa Road section, central Italy. *Earth and Planetary Science Letters* 290, 192–200.
- Gingerich, P.D., 2006. Environment and evolution through the Paleocene-Eocene thermal maximum. *Trends in ecology & evolution* 21, 246–53.
- Gingerich, P. D., 2010. Mammalian faunal succession through the Paleocene-Eocene thermal maximum (PETM) in western North America. *Vertebrata Palasiatica*, 48, 308–327.
- González-Bonorio, G., Colombo, F., Abascal, L., 2010. Architecture of an Oligocene fluvial ribbon sandstone in the Ebro Basin, North-eastern Spain. *Sedimentology* 57, 845–8.
- Gradstein, F.M., Ogg, J.G., Schmitz, M.D., and Ogg, G.M., 2012, *The Geologic Time Scale 2012*, Vol. 1: Boston, Elsevier.
- Hajek, E. A., Heller, P. L., and Sheets, B.A., 2010. Significance of channel-belt clustering in alluvial basins. *Geology*, 38, 535–538.
- Hammer, Ø., Harper, D., 2001. PAST: Paleontological statistics software package for education and data analysis. *Palaeo. Electronica* 4, 1–9.
- Higgins, J. A., Schrag, D.P., 2006. Beyond methane: Towards a theory for the Paleocene–Eocene Thermal Maximum. *Earth and Planetary Science Letters* 245, 523–537.
- Hilgen, F.J., Kuiper, K.F., Lourens, L.J., 2010. Evaluation of the astronomical time scale for the Paleocene and earliest Eocene. *Earth and Planetary Science Letters* 300, 139–151.
- Jackson, D., 1993. Stopping rules in principal components analysis: a comparison of heuristical and statistical approaches. *Ecology* 74, 2204–2214.
- Kennett, J.P., Stott, L.D., 1991. Abrupt deep-sea warming, palaeoceanographic changes and benthic extinctions at the end of the Palaeocene. *Nature* 353, 225–229.
- Kent, D.V., Cramer, B.S., Lanci, L., Wang, D., Wright, J.D., Van der Voo, R., 2003. A case for a comet impact trigger for the Paleocene/Eocene thermal maximum and carbon isotope excursion. *Earth and Planetary Science Letters* 211, 13–26.
- Kirschvink, J.L., 1980. The least-squares line and plane and the analysis of palaeomagnetic data. *Geophysical Journal, Royal Astronomical Society* 62, 699–718.
- Koch, P., Zachos, J., Gingerich, P., 1992. Correlation between isotope records in marine and continental carbon reservoirs near the Paleocene Eocene boundary. *Nature* 358, 319–322.
- Kraus, M.J., 1987. Integration of channel and floodplain suites; II, vertical relations of alluvial paleosols. *Journal of Sedimentary Research* 57, 602–612.
- Kraus, M. J., 1996. Avulsion deposits in lower Eocene alluvial rocks, Bighorn Basin, Wyoming. *Journal of Sedimentary Research* 66, 354–363.
- Kraus, M. J., Aslan, A., 1993. Eocene hydromorphic paleosols: significance for interpreting ancient floodplain processes. *Journal of Sedimentary Research* 63, 453–463.
- Kraus, M. J., Riggins, S., 2007. Transient drying during the Paleocene–Eocene Thermal Maximum (PETM): Analysis of paleosols in the bighorn basin, Wyoming. *Palaeogeography, Palaeoclimatology, Palaeoecology* 245, 444–461.
- Kuiper, K.F., Deino, A., Hilgen, F.J., Krijgsman, W., Renne, P.R.,

- Wijbrans, J.R., 2008. Synchronizing the rock clocks of Earth history. *Science* 320, 500–504.
- Kurtz, A.C., Kump, L.R., Arthur, M.A., Zachos, J., Paytan, A., 2003. Early Cenozoic decoupling of the global carbon and sulfur cycles. *Paleoceanography* 18, 14–1.
- Laskar, J., Gastineau, M., Delisle, J., Farrés, A., Fienga, A., 2011. Strong chaos induced by close encounters with Ceres and Vesta. *Astronomy & Astrophysics* 532, L4.
- Lourens, L.J., Sluijs, A., Kroon, D., Zachos, J.C., Thomas, E., Röhl, U., Bowles, J., Raffi, I., 2005. Astronomical pacing of late Palaeocene to early Eocene global warming events. *Nature* 435, 1083–1087.
- McInerney, F., Wing, S.L., 2011. The Paleocene-Eocene Thermal Maximum: A Perturbation of Carbon Cycle, Climate, and Biosphere with Implications for the Future. *Annual Review of Earth and Planetary Sciences* 39, 489–516.
- Murphy, B.H., Farley, K., Zachos, J.C., 2010. An extraterrestrial ^3He -based timescale for the Paleocene–Eocene thermal maximum (PETM) from Walvis Ridge, IODP Site 1266. *Geochimica et Cosmochimica Acta* 74, 5098–5108.
- Paillard, D., Labeyrie, L., Yiou, P., 1996. Macintosh Program performs time-series analysis. *Eos, Transactions American Geophysical Union* 77, 379.
- Renne, P.R., Deino, A., Hilgen, F.J., Kuiper, K.F., Mark, D.F., Mitchell III, W.S., Morgan, L.E., Mundil, R., Smit, J., 2013. Time scales of critical events around the Cretaceous-Paleogene boundary. *Science* 339, 684–687.
- Schoeneberger, P. J., Wysocki, D., Benham, E. & Broderson, W., 2002. Field book for describing and sampling soils. National Soil Survey Center, Natural Resources Conservation Service, US Dept. of Agriculture.
- Schubert, B., Jahren, H., 2012. The effect of atmospheric CO₂ concentration on carbon isotope fractionation in C3 land plants. *Geochimica et Cosmochimica Acta* 96, 29–43.
- Schulz, M., Mudelsee, M., 2002. REDFIT: estimating red-noise spectra directly from unevenly spaced paleoclimatic time series. *Computers & Geosciences* 28, 421–426.
- Sexton, P.F., Norris, R.D., Wilson, P. A, Pälike, H., Westerhold, T., Röhl, U., Bolton, C.T., Gibbs, S., 2011. Eocene global warming events driven by ventilation of oceanic dissolved organic carbon. *Nature* 471, 349–52.
- Sluijs, A., Dickens, G.R., 2012. Assessing offsets between the $\delta^{13}\text{C}$ of sedimentary components and the global exogenic carbon pool across early Paleogene carbon cycle perturbations. *Global Biogeochemical Cycles* 26, GB4005.
- Stap, L., Lourens, L.J., Thomas, E., Sluijs, A., Bohaty, S., Zachos, J.C., 2010. High-resolution deep-sea carbon and oxygen isotope records of Eocene Thermal Maximum 2 and H2. *Geology* 38, 607–610.
- Stap, L., Sluijs, A., Thomas, E., Lourens, L.J., 2009. Patterns and magnitude of deep sea carbonate dissolution during Eocene Thermal Maximum 2 and H2, Walvis Ridge, southeastern Atlantic Ocean. *Paleoceanography* 24, 1–13.
- Svensen, H., Planke, S., Malthe-Sørenssen, A., 2004. Release of methane from a volcanic basin as a mechanism for initial Eocene global warming. *Nature* 429, 3–6.
- Tauxe, L., Gee, J., Gallet, Y., Pick, T., Bown, T., 1994. Magnetostratigraphy of the Willwood Formation, Bighorn Basin, Wyoming: new constraints on the location of Paleocene/Eocene boundary. *Earth and Planetary Science Letters* 125, 159–172.
- Thomas, E., Shackleton, N., 1996. The Paleocene-Eocene benthic foraminiferal extinction and stable isotope anomalies. *Geological Society, London, Special Publications* 101, 401–441.
- Westerhold, T., Röhl, U., Laskar, J., 2012. Time scale controversy: Accurate orbital calibration of the early Paleogene. *Geochemistry Geophysics Geosystems* 13, 1–19.
- Westerhold, T., Röhl, U., Laskar, J., Raffi, I., Bowles, J., Lourens, L.J., Zachos, J.C., 2007. On the duration of magnetochrons C24r and C25n and the timing of early Eocene global warming events: Implications from the Ocean Drilling Program Leg 208 Walvis Ridge depth transect. *Paleoceanography* 22, 1–19.
- Yperen, van, A. 2012. Cyclostratigraphic framework for the ETM2 and H2 hyperthermals in the Willwood Formation, Bighorn Basin, Wyoming (USA). University Utrecht (master thesis).
- Zachos, J.C., Lohmann, K., Walker, J., C.G., Wise, S.W., 1993. Abrupt climate change and transient climates during the Paleogene: A marine perspective. *The Journal of Geology*, 101(2), 191–213.
- Zachos, J.C., Röhl, U., Schellenberg, S. a, Sluijs, A., Hodell, D., Kelly, D.C., Thomas, E., Nicolo, M., Raffi, I., Lourens, L.J., McCarren, H., Kroon, D., 2005. Rapid acidification of the ocean during the Paleocene-Eocene thermal maximum. *Science* 308, 1611–5.
- Zeebe R.E., Zachos J. C., Dickens G.R., 2009. Carbon dioxide forcing alone insufficient to explain Palaeocene–Eocene Thermal Maximum warming. *Nature Geoscience* 2, 576–580.
- Zijderveld, J. D. A. 1967. A. C. demagnetization of rocks: analysis of results. In: Runcorn, S. K. (ed.) *Methods in Palaeomagnetism*. Elsevier, 254–286.

APPENDIX 1 – Paleomagnetic results for the ChRM components

Sample	Level	Dec	inc	Temp. range	Sample	Level	Dec	inc	Temp. range
WB Section					CSH Section				
WBP 2	-19	351	63	510-640	CSH-2	-33,0	162	-12	430-550
WBP 3	-18,6	357	64	510-640	CSH-11	-21,0	138	-72	460-570
WBP 5A	-15,6	143	-11	510-710 (-540)	CSH-29	12,4	233	14	520-570
WBP 10	-10,75	171	-65	540-640	CSH-30	13,1	140	-16	490-570
WBP 17	-4,1	376	58	510-590	CSH-26	17,7	244	32	460-570
WBP 12	-9,25	131	-59	540-710(-690)	CSH-25	19,6	149	-29	460-570
WBP 15	-6,625	140	-36	300-570					
WBP 19	2,7	350	68	480-670					
WBP 30	19,5	191	-64	480-570					
WBP 31	20,375	182	-37	610-710					
WBP 32	23,125	264	-65	510-610					
WBP 34	25,5	112	-42	670-710 (-690)					
WBP 37A	34,25	139	-7	510-610					
WBP 38	35,875	115	-30	590-540					
WBP 40	39,25	136	-22	590-670					
WBP 46	49,125	314	63	480-640					
WBP 48	51,25	343	59	510-640					
WBP 55	58,125	246	4	510-710					
WBP 63	92	344	57	480-640					
WBP 64	94,125	363	73	570-710					
WBP 66	132,87	325	73	480-640					
WBP 72	148	175	-66	540-640					
WBP 75	152,12	338	81	510-710					
UDC Section									
EDC0	54,15	310	68	450-510					
EDC2	55,65	340	57	480-600					
EDC20-1	53,12	296	57	450-600					
EDC26-2	49,95	352	63	450-600 (-480)					
EDC27-1	48,9	372	61	480-600					
EDC41	40,5	346	61	450-510					
EDC46-2	36,05	176	-26	480-600					
EDC47-1	35,35	151	-37	480-600					
EDC52	30,75	134	-13	450-570					
EDC58	26,7	149	-44	480-600					
EDC59	26,35	130	-48	450-600					
EDC6	320,6	172	-6	540-600					
EDC69	13,160	101	-37	540-600					
EDC96	-39,7	137	-13	480-600					
EDC97	-40,32	125	-51	480-600					
EDC110	-54	151	-64	510-600					
EDC112	-57,1	206	-44	510-600					
EDC118	-66,58	167	-22	5480-600					

APPENDIX 2 – Carbon and oxygen isotope values from micritic carbonate from the WB section in the McCullough Peaks, Bighorn Basin

Sample	Level	$\delta^{13}\text{C}$	$\delta^{18}\text{O}$	Sample	Level	$\delta^{13}\text{C}$	$\delta^{18}\text{O}$
WBS 2.1	0,5	-10,186	-8,688	WBS 153.1	38,25	-10,256	-8,548
WBS 4.2	1	-10,718	-8,425	WBS 156.1	39	-10,29	-8,263
WBS 4.1	1	-10,009	-8,482	WBS 156.2	39	-10,161	-8,213
WBS 6.1	1,5	-10,144	-8,623	WBS 158A.11	39,62	-9,784	-8,596
WBS 15.1	3,75	-11,449	-7,678	WBS 160,1	40	-9,138	-8,477
WBS 18A.1	4,625	-11,619	-13,46	WBS 162.1	40,5	-8,753	-8,284
WBS 21.1	5,25	-10,594	-8,808	WBS 165,1	41,25	-10,491	-9,310
WBS 23.1	5,75	-10,864	-9,392	WBS 168.1	42	-9,642	-8,771
WBS 24A.1	6,125	-10,655	-8,337	WBS 172.1	43	-9,835	-9,151
WBS 26.1	6,5	-10,703	-8,347	WBS 174.1	43,5	-9,686	-8,267
WBS 28A.2.5	7,125	-11,979	-15,77	WBS 176,1	44	-9,672	-8,316
WBS 28A.2	7,125	-11,087	-8,958	WBS 179A.1	44,875	-9,867	-8,036
WBS 28A.1	7,125	-10,969	-8,634	WBS 182.1	45,5	-9,631	-8,148
WBS 30A.1	7,625	-10,791	-8,434	WBS 185.1	46,25	-10,101	-8,700
WBS 40A.1	10,125	-11,243	-8,297	WBS 192.1	48	-12,055	-8,360
WBS 43A.1	10,875	-12,410	-8,610	WBS 196.1	49	-12,074	-8,339
WBS 47.1	11,75	-12,963	-8,698	WBS 196.2	49	-11,617	-8,423
WBS 49.1	12,25	-12,137	-8,435	WBS 197.1	49,25	-13,646	-8,348
WBS 51.1	12,75	-12,611	-8,881	WBS 199.1	49,75	-11,613	-8,611
WBS 57.1	14,25	-13,317	-9,163	WBS 201.1	50,25	-8,182	-9,109
WBS 59.1	14,75	-12,756	-8,892	WBS 204.1	51,125	-10,604	-8,677
WBS 69.1	17,25	-12,369	-8,022	WBS 207.1	51,75	-6,553	-9,824
WBS 71.1	17,75	-11,288	-7,756	WBS 211A.5	52,875	-12,292	-16,662
WBS 76.1	19	-12,810	-8,383	WBS 211A.1	52,875	-9,499	-9,330
WBS 78,1	19,5	-13,188	-8,610	WBS 211A.1	52,875	-9,414	-8,896
WBS 80,1	20	-9,987	-8,227	WBS 214.1	53,5	-9,752	-8,300
WBS 81.1	20,25	-9,505	-8,190	WBS 220A.1	55,125	-10,301	-8,283
WBS 86.1	21,5	-11,262	-8,289	WBS 224.1	56	-10,181	-8,406
WBS 89A.1	22,375	-11,663	-9,327	WBS 225A.1	56,375	-10,364	-8,852
WBS 95.1	23,75	-11,617	-8,357	WBS 225a.2	56,375	-10,214	-8,469
WBS 98A.1	24,625	-12,631	-9,005	WBS 227.1	56,75	-9,709	-8,345
WBS 98A.2	24,625	-11,481	-8,998	WBS 231.1	57,75	-12,224	-8,878
WBS 100.1	25	-11,297	-8,567	WBS 234.1	58,5	-9,441	-8,662
WBS 104.1	26	-13,082	-8,545	WBS 236A.1	59,125	-9,996	-8,314
WBS 111.1	27,75	-10,865	-8,262	WBS 238.1	59,5	-9,555	-8,596
WBS 119.1	29,75	-10,422	-8,404	WBS 239A.1	59,875	-10,976	-10,911
WBS 123.1	30,75	-9,799	-8,646	WBS 244.1	61	-10,706	-8,530
WBS 129.1	32,25	-9,826	-8,473	WBS 247.1	61,75	-10,358	-8,416
WBS 132A.1	33,125	-9,945	-8,521	WBS 247.2	61,75	-9,921	-8,339
WBS 135.1	33,75	-10,079	-9,132	WBS 251A.1	62,875	-9,026	-9,476
WBS 140.1	35	-10,415	-9,076	WBS 257.1	64,25	-9,506	-10,015
WBS 143.1	35,75	-9,373	-8,338	WBS 265.1	66,25	-10,509	-8,900
WBS 145A.1	36,375	-9,226	-8,377	WBS 267.1	66,75	-9,773	-8,576
WBS 147.1	36,75	-10,132	-8,873	WBS 274.1	68,5	-14,125	-9,354
WBS 149A.1	37,375	-9,749	-8,309	WBS 278.1	69,5	-9,742	-8,686
WBS 149A.2	37,375	-9,621	-8,522	WBS 283.1	70,75	-10,412	-8,312
WBS 152.1	38	-10,291	-8,598	WBS 286.1	71,5	-10,732	-8,470

Sample	Level	$\delta^{13}\text{C}$	$\delta^{18}\text{O}$	Sample	Level	$\delta^{13}\text{C}$	$\delta^{18}\text{O}$
WBS 289.1	72,25	-10,447	-8,361	WBS 452.2	113	-11,583	-8,123
WBS 289.2	72,25	-10,393	-8,455	WBS 455.1	113,75	-11,638	-8,360
WBS 291.1	72,75	-10,657	-8,683	WBS 458.1	114,5	-11,103	-8,320
WBS 295.1	73,75	-10,434	-8,788	WBS 462.1	115,5	-11,020	-9,752
WBS 298.1	74,5	-9,951	-9,439	WBS 466.1	116,5	-11,753	-8,125
WBS 315.1	78,75	-10,212	-9,914	WBS 468.1	117	-10,973	-7,930
WBS 320.1	80	-10,465	-9,701	WBS 469A.1	117,375	-10,974	-7,866
WBS 325A.1	81,375	-10,689	-9,411	WBS 471.1	117,75	-11,211	-8,074
WBS 328.1	82	-10,858	-10,353	WBS 473.2	118,25	-10,635	-8,143
WBS 329A.2	82,375	-9,631	-8,418	WBS 473.1	118,25	-10,364	-8,143
WBS 329A.2	82,375	-9,178	-8,332	WBS 476.1	119	-10,130	-8,356
WBS 330.1	82,5	-9,769	-8,488	WBS 478A.1	119,625	-9,918	-8,551
WBS 333.1	83,25	-10,635	-9,833	WBS 482A.1	120,625	-10,089	-8,655
WBS 334A.1	83,625	-9,245	-8,615	WBS 484.1	121	-9,850	-8,779
WBS 337.1	84,25	-8,848	-8,472	WBS 497.1	124,25	-9,276	-9,077
WBS 340.1	85	-9,527	-8,280	WBS 500.1	125	-9,430	-8,465
WBS 342.2	85,5	-9,564	-8,288	WBS 500A.1	125,125	-9,692	-8,525
WBS 346.1	86,5	-15,342	-12,273	WBS 501.1	125,25	-9,410	-8,307
WBS 356.1	89	-9,615	-8,003	WBS 505.1	126,25	-10,622	-8,203
WBS 357.1	89,25	-8,994	-8,569	WBS 506.1	126,5	-10,487	-8,379
WBS 361.1	90,25	0,033	0,065	WBS 507.1	126,75	-10,342	-7,982
WBS 366A.1	91,625	-11,981	-8,510	WBS 509.1	127,25	-10,811	-8,218
WBS 368A.1	92,125	-11,306	-8,369	WBS 512.1	128	-11,005	-8,409
WBS 372.1	93	-11,277	-7,913	WBS 513.1	128,25	-10,569	-8,429
WBS 372.2	93	-11,182	-8,015	WBS 513.1	128,25	-10,511	-9,222
WBS 374.1	93,5	-6,878	-7,446	WBS 516A.1	129	-11,051	-8,414
WBS 385.1	96,25	-12,541	-7,733	WBS 517.1	129,25	-11,705	-8,445
WBS 387.1	96,75	-12,467	-7,980	WBS 526.1	131,5	-11,223	-7,957
WBS 389.1	97,25	-12,239	-7,848	WBS 527.1	131,75	-11,458	-8,315
WBS 390.1	97,5	-12,735	-7,660	WBS 533.1	133,25	-11,369	-8,157
WBS 394.1	98,5	-12,947	-8,277	WBS 533.2	133,25	-10,971	-8,418
WBS 398A.2	99,625	-12,680	-8,407	WBS 536.1	134	-11,188	-8,184
WBS 398A.1	99,625	0,303	0,580	WBS 539.1	134,75	-11,378	-8,404
WBS 401.1	100,25	-12,325	-7,827	WBS 541.1	135,25	-10,577	-8,577
WBS 405.1	101,25	-12,281	-8,202	WBS 542.1	135,5	-10,982	-8,564
WBS 407.1	101,75	-12,696	-7,806	WBS 551.1	137,75	-11,755	-8,659
WBS 408.1	102	-13,107	-8,268	WBS 554.1	138,5	-10,129	-7,587
WBS 408.2	102	-11,774	-9,122	WBS 557.1	139,25	-12,188	-9,025
WBS 413A.1	103,375	-13,336	-10,108	WBS 559.1	139,75	-10,866	-7,828
WBS 416.1	104	-12,098	-8,844	WBS 561.1	140,25	-11,350	-9,092
WBS 422.1	105,5	-11,801	-8,679	WBS 564A.1	141,125	-11,469	-8,824
WBS 426.1	106,5	-11,751	-8,874	WBS 566.1	141,5	-10,918	-8,067
WBS 426.2	106,5	-11,742	-8,885	WBS 568.1	142	-11,992	-8,691
WBS 428.2	107	-9,629	-7,593	WBS 568.2	142	-11,548	-8,588
WBS 428.1	107	-9,612	-7,286	WBS 568.11	142	-9,544	-8,629
WBS 430.1	107,5	-10,875	-7,541	WBS 588.1	147	-9,794	-8,954
WBS 434.1	108,5	-11,446	-8,471	WBS 590.1	147,5	-9,534	-9,402
WBS 440A.1	110,125	-12,635	-8,431	WBS 597.1	149,25	-9,198	-8,549
WBS 447.1	111,75	-11,100	-8,108	WBS 597A.1	149,375	-9,807	-8,521
WBS 449A.1	112,375	-11,385	-8,006	WBS 603.1	150,75	-11,552	-9,415
WBS 452.1	112,75	-11,312	-7,841	WBS 606A.1	151,625	-10,597	-8,37
WBS 608.1	152	-10,223	-8,171	WBS 607.2	151,75	-10,457	-8,576
WBS 611.1	152,75	-10,535	-9,649	WBS 607.2	151,75	-10,406	-8,738
WBS 613.1	153,25	-10,449	-8,306				

Sample	Level	$\delta^{13}\text{C}$	$\delta^{18}\text{O}$	Sample	Level	$\delta^{13}\text{C}$	$\delta^{18}\text{O}$
WBS 613.2	153,25	-10,364	-8,253	13,1	-2,55	-12,00	-8,68
WBS 615.1	153,75	-10,185	-8,112	14	-4,2	-11,31	-7,96
WBS 616.1	154	-10,908	-8,362	15,1	-4,95	-12,79	-8,49
WBS 619A.1	154,87	-9,766	-8,314	16	-4,85	-12,39	-8,18
WBS 622.1	155,5	-10,135	-10,096	17	-4,7	-11,52	-7,98
WBS 632.1	158	-10,023	-8,555	12,1	-2,7	-10,30	-8,53
WBS 634.1	158,5	-9,401	-8,320	18,1	-4,4	-11,19	-8,15
WBS 637A.1	159,37	-9,899	-8,153	20,1	-3,85	-11,61	-8,38
WBS 640.1	160	-10,084	-8,334	21,1	-8,05	-13,05	-8,54
WBS 642.1	160,5	-10,086	-8,437	22,1	-7,9	-13,03	-8,70
WBS 642.2	160,5	-8,149	-8,293	23,1	-7,2	-12,93	-8,61
WBS 643.1	160,75	-9,022	-8,214	24,1	-9,2	-13,03	-9,05
WBS 645.1	161,25	-9,334	-8,663	25	-11,6	-13,58	-7,61
WBS 646.1	161,5	-10,106	-8,933	26,1	-11,45	-13,46	-8,34
WBS 659.1	164,75	-9,572	-8,761	27,1	-10,95	-13,03	-8,28
WBS 662A.1	165,62	-9,210	-8,460	28	-10,7	-13,31	-8,24
WBS 664.1	166	-9,143	-8,579	29,1	-10,45	-13,15	-8,30
WBS 671.1	167,75	-10,094	-9,296	33,1	-14,65	-14,06	-8,79
WBS 677.2	169,25	-9,461	-8,993	36,1	-14,2	-14,19	-8,88
WBS 677.1	169,25	-9,417	-9,035	38,1	-13,85	-14,37	-8,66
WBS 682.1	170,5	-9,672	-9,174	40,1	-13,45	-14,09	-8,65
WBS 684.1	171	-9,970	-8,721	42,1	-17,45	-13,87	-8,88
WBS 699.1	174,75	-9,133	-9,478	43,1	-19,35	-11,04	-9,33
WBS 709A.1	177,37	-10,286	-8,903	46,1	-20,35	-12,03	-8,90
WBS 712.1	178	-10,773	-9,102	47,1	-20,05	-11,67	-8,41
WBS 714A.1	178,62	-10,246	-8,446				
WBS 714A.1	178,62	-10,225	-8,433				
WBS 719.1	179,75	-9,356	-8,870				
WBS 722.1	180,5	-9,597	-8,834				
WBS 730A.1	182,5	-11,031	-9,007				
WBS 733.1	183,25	-9,893	-9,402				
WBS 737.1	184,25	-9,820	-9,523				
WBS 739.1	184,75	-10,668	-8,489				
WBS 739.1	184,75	-10,324	-8,307				
WBS 741.1	185,25	-10,903	-9,107				
WBS 742.1	185,5	-12,446	-11,310				

Spar Measurements

WBS 28A.2.5	-11,979	-15,777
WBS 211A.5	-12,301	-16,662
WBS 261.5	-12,014	-16,185

Measurements From Van den Berg (2012)

1,1	2,5	-12,79	-10,17
3,1	-0,35	-10,25	-8,45
3,1	-0,35	-10,21	-8,44
6,1	0,05	-10,41	-8,62
7,1	0,55	-10,40	-9,46
8,1	-1,85	-10,69	-8,60
9,1	-1,7	-11,17	-9,14
10	-3,35	-11,29	-8,44
10	-3,35	-11,33	-8,42
11,1	-3,2	-11,43	-8,53
11,1	-3,2	-11,42	-8,57

APPENDIX 3 – Carbon and oxygen isotope values from micritic carbonate from the DCA section in the McCullough Peaks, Bighorn Basin

Sample	Level	$\delta^{13}\text{C}$	$\delta^{18}\text{O}$	Sample	Level	$\delta^{13}\text{C}$	$\delta^{18}\text{O}$
DCASA 1.1	0	-9,790	-9,172	DCASA 137.1	27,4	-10,196	-8,214
DCASA 3.1	0,6	-10,24	-8,7	DCASA 147.1	29,2	-10,583	-8,173
DCASA 6.1	1	-9,628	-8,155	DCASA 151.1	30	-10,23	-8,2
DCASA 7.1	1,200	-9,826	-8,374	DCASB 3.1	32,6	-10,03	-9,7
DCASA 8.1	1,4	-9,790	-8,839	DCASB 3.2	32,6	-9,92	-9,2
DCASA 8.2	1,4	-9,733	-8,556	DCASB 8.1	33,6	-9,946	-8,437
DCASA 9.1	1,6	-9,609	-8,317	DCASB 8.2	33,6	-9,806	-8,454
DCASA 13.1	2,4	-9,794	-8,348	DCASB 18.1	35,6	-11,09	-9,0
DCASA 13.2	2,4	-9,726	-8,399	DCASB 18.2	35,6	-10,51	-8,0
DCASA 25.1	4,8	-9,74	-9,6	DCASB 19.1	35,8	-11,11	-7,9
DCASA 28.1	5,4	-10,105	-8,444	DCASB 20.1	36	-10,491	-7,747
DCASA 41.1	8	-9,162	-8,576	DCASB 23.2	36,6	-10,993	-8,040
DCASA 41.2	8	-8,770	-8,477	DCASB 23.1	36,6	-10,633	-8,010
DCASA 43.1	8,4	-9,566	-8,959	DCASB 36.1	39,2	-9,90	-8,3
DCASA 44.1	8,6	-8,99	-8,3	DCASB 52.1	42,4	-9,617	-8,669
DCASA 44.2	8,6	-10,07	-8,7	DCASB 57.1	43,4	-10,598	-9,417
DCASA 46.1	9	-9,51	-7,7	DCASB 60.1	44	-9,930	-8,641
DCASA 58.2	11,4	-9,315	-8,464	DCASB 62.1	44,4	-9,82	-8,6
DCASA 58.1	11,4	-9,543	-8,611	DCASB 62.2	44,4	-9,95	-8,7
DCASA 68.1	13,4	-9,686	-8,179	DCASB 67.1	45,4	-10,008	-8,256
DCASA 68.2	13,4	-10,246	-9,409	DCASB 67.2	45,4	-9,882	-8,458
DCASA 70.1	13,8	-10,722	-9,422	DCASB 67.2d	45,4	-9,880	-8,527
DCASA 78.1	15,4	-9,308	-8,979	DCASB 71.2	46,2	-10,789	-8,1
DCASA 79.1	15,6	-10,264	-8,510	DCASB 71.1	46,2	-10,546	-8,065
DCASA 80.1	15,8	-9,93	-8,3	DCASB 71.2	46,2	-10,532	-7,740
DCASA 80.2	15,8	-9,62	-8,2	DCASB 72.1	46,4	-10,292	-8,449
DCASA 80.2d	15,8	-9,59	-8,2	DCASB 72.2	46,4	-10,344	-8,083
DCASA 81.1	16	-9,07	-8,1	DCASB 73.2	46,6	-10,158	-8,1
DCASA 82.1	16,2	-10,760	-8,754	DCASAB 73.1	46,6	-10,07	-8,3
DCASA 83.1	16,4	-9,46	-8,0	DCASB 74.1	46,8	-9,925	-9,450
DCASA 93.1	18,4	-9,964	-8,324	DCASB 74.1d	46,8	-9,697	-9,144
DCASA 96.1	19	-10,848	-8,666	DCASB 75.1	47	-9,51	-8,7
DCASA 96.2	19	-10,507	-8,443	DCASB 75.2	47	-9,45	-9,4
DCASA 105.1	20,8	-9,941	-8,291	DCASB 76.1	47,2	-9,574	-8,969
DCASA 105.2	20,8	-9,941	-8,294	DCASB 77.1	47,4	-9,455	-8,6
DCASA 118.1	23,4	-9,522	-8,181	DCASB 77.2	47,4	-10,06	-8,4
DCASA 119.1	23,6	-9,33	-8,1	DCASB 79.1	47,8	-9,196	-8,8
DCASA 119.2	23,6	-9,31	-8,2	DCASB 79.2	47,8	-9,51	-8,7
DCASA 120,1	23,8	-9,77	-8,5	DCASB 92.1	50,6	-9,296	-8,510
DCASA 127.1	25,2	-10,208	-8,122	DCASB 100.1	52,2	-10,87	-9,0
DCASA 128.1	25,4	-10,252	-8,033	DCASB 102.1	52,6	-10,234	-8,627
DCASA 129.1	25,6	-10,16	-8,2	DCASB 106.1	53,4	-10,814	-8,967
DCASA 129.2	25,6	-10,06	-8,3	DCASB 111.1	54,2	-10,58	-8,4
DCASA 130.1	25,8	-10,402	-8,245	DCASB 111.2	54,2	-10,138	-8,4
DCASB 112.1	54,4	-10,14	-8,9	DCASC 71.1	78,2	-10,712	-8,1
DCASB 114.1	54,8	-10,408	-8,438	DCASC 72.1	78,4	-10,186	-7,840
DCASB 128.1	57,6	-11,091	-9,126	DCASC 86.1	81,2	-9,475	-8,3
DCASB 93.1	60,8	-10,186	-8,824	DCASC 86.2	81,2	-8,76	-8,4
DCASB 155.1	63,2	-10,315	-8,261	DCASC 89.1	81,8	-9,228	-8,279
DCASC 3.1	64,6	-9,49	-8,4	DCASC 90.1	82	-10,291	-8,870
DCASC 3.2	64,6	-9,42	-8,5	DCASC 90.2	82	-10,324	-8,868

Sample	Level	$\delta^{13}\text{C}$	$\delta^{18}\text{O}$	Sample	Level	$\delta^{13}\text{C}$	$\delta^{18}\text{O}$
DCASC 3.2	64,6	-9,42	-8,5	DCASC 105.1	85,0	-9,815	-8,7
DCASC 4.1	64,8	-10,158	-7,963	DCASC 105.2	85,0	-9,830	-8,6
DCASC 9.1	65,8	-9,478	-8,548	DCASC 106.2	85,2	-14,203	-9,3
DCASC 10.1	66	-9,50	-9,2	DCASD 10.1	88	-10,133	-8,848
DCASC 12.1d	66,4	-9,583	-8,377	DCASD 10.2	88	-10,420	-9,376
DCASC 12.1	66,4	-9,600	-8,268	DCASD 15.1	89	-10,298	-7,992
DCASC 12.2	66,4	-9,473	-8,185	DCASD 16.1	89,2	-10,577	-8,138
DCASC 14.1	66,8	-9,42	-8,3	DCASC 17.1	89,4	-10,691	-7,977
DCASC 17.1	67,4	-9,966	-8,199	DCASD 18.1	89,6	-10,447	-8,300
DCASC 23.1	68,6	-12,939	-8,356	DCASD 18.2	89,6	-10,321	-7,850
DCASC 30.1	70	-9,058	-7,462	DCASD 19.2	89,8	-10,417	-8,553
DCASC 31.1	70,2	-7,955	-7,787	DCASD 19.1	89,8	-10,168	-8,073
DCASC 35.1	71	-9,521	-7,989	DCASD 33.1	92,6	-9,590	-8,038
DCASC 38.1	71,6	-11,876	-9,131	DCASD 33.4	92,6	-9,834	-7,801
DCASC 40.1	72	-10,517	-8,553	DCASD 34.1	92,8	-9,621	-8,4
DCASC 40.2	72	-9,758	-8,381	DCASD 34.2	92,8	-9,871	-8,5
DCASC 41.1	72,2	-8,985	-8,4	DCASD 35.2	93	-9,210	-8,217
DCASC 41.2	72,2	-9,697	-8,2	DCASD 35.1	93	-9,549	-7,972
DCASC 46.1	73,2	-10,116	-8,4	DCASD 36.2	93,2	-8,996	-8,546
DCASC 46.2	73,2	-11,333	-9,8	DCASD 36.2	93,2	-8,996	-8,546
DCASC 47.1	73,4	-10,580	-8,313	DCASD 36.2	93,2	-8,996	-8,546
DCASC 47.13	73,4	-10,346	-8,103	DCASD 36.1	93,2	-9,822	-8,938
DCASC 47.2	73,4	-10,738	-8,760	DCASD 37.1	93,4	-9,003	-8,221
DCASC 49.1	73,8	-10,516	-8,8	DCASD 38.1	93,6	-8,927	-8,233
DCASC 49.2	73,8	-11,221	-8,4	DCASD 38.2	93,6	-9,006	-8,4
DCASC 50.1	74	-10,70	-8,4	DCASD 39.1	93,8	-9,472	-9,3
DCASC 50.2	74	-10,169	-8,8	DCASD 39.2	93,8	-9,290	-9
DCASC 51.1	74,2	-7,510	-7,5	DCASD 39.4	93,8	-9,315	-8,3
DCASC 51.2	74,2	-7,710	-8,4	DCASD 40.1	94	-10,146	-9,3
DCASC 52.1	74,4	-11,209	-8,343	DCASD 40.2	94	-10,230	-9,0
DCASC 52.2	74,4	-9,421	-8,176	DCASD 42.1	94,4	-9,303	-8,8
DCASC 53.1	74,6	-10,066	-8,7	DCASD 43.1	94,6	-9,914	-8,585
DCASC 53.2	74,6	-10,176	-8,8	DCASD 49.1	95,8	-9,472	-8,754
DCASC 60.1	76	-10,428	-7,834	DCASD 49.2	95,8	-9,543	-8,075
DCASC 63.1	76,6	-11,37	-8,3	DCASD 50.1	96	-9,954	-8,340
DCASC 64.1	76,8	-11,386	-7,9	DCASD 53.1	96,6	-10,049	-8,089
DCASC 64.2	76,8	-9,77	-8,5	DCASD 54.1	96,8	-9,197	-8,248
DCASC 65.1	77	-10,152	-8,4	DCASD 54.2	96,8	-8,968	-8,274
DCASC 65.2	77	-10,55	-8,3	DCASD 56.1	97,2	-11,226	-9,529
DCASC 68.1	77,6	-10,284	-8,580	DCASD 59.1	97,8	-9,139	-8,6
DCASC 94.1	82,8	-9,775	-8,289	DCASD 59.2	97,8	-9,577	-8,6
DCASC 94.2	82,8	-10,275	-9,954	DCASD 60.1	98	-8,844	-8,4
DCASC 95.1	83	-12,439	-9,3	DCASD 66.1	99,2	-18,026	-13,599
DCASC 95.2	83	-10,09	-8,3	DCASD 82.1	102,4	-11,012	-9,1
DCASC 96.1	83,2	-10,585	-8,0	DCASD 90.1	104	-9,757	-7,957
DCASC 96.2	83,2	-10,17	-7,9	DCASD 90.2	104	-9,708	-7,916
DCASC 97.1	83,4	-10,41	-7,9	DCASD 91.1	104,2	-9,658	-7,831
DCASC 97.2	83,4	-10,382	-8,1	DCASD 91.2	104,2	-8,672	-8,210
DCASC 98.1	83,6	-10,65	-7,9	DCASD 92.1	104,4	-9,674	-7,873
DCASC 98.2	83,6	-10,418	-7,7	DCASD 92.2	104,4	-9,725	-8,020
DCASC 99.1	83,8	-9,83	-8,3	DCASD 93.1	104,6	-8,637	-7,881
DCASC 99.2	83,8	-10,33	-8,0	DCASD 93.2	104,6	-9,494	-8,038
DCASC 100.1	84	-10,420	-8,001	DCASD 105.1	107	-9,487	-9,509
DCASC 100.2	84	-10,441	-8,211	DCASD 105.2	107	-9,527	-8,829
DCASC 103.1	84,6	-10,271	-9,286	DCASD 106.1	107,2	-9,544	-9
DCASD 106.2	107,2	-10,132	-10,308	DCASD 108.1	107,6	-9,951	-9,0

Sample	Level	δ13C	δ18O
DCASD 108.2	107,6	-10,200	-9,4
DCASD 110.1	108	-11,019	-8,869
DCASD 114.1	108,8	-10,016	-8,812
DCASD 131.1	112,2	-10,674	0,297
DCASD 136.1	113,2	-10,569	-8,496
DCASD 143.1	114,6	-9,119	-8,179
DCASD 143.2	114,6	-9,620	-9,296
DCASD 145.1	115	-9,100	-7,992
DCASD 145.2	115	-9,017	-8,158
DCASD 146.1	115,2	-9,080	-8,306
DCASD 147.1	115,4	-9,537	-8,511
DCASD 149.1	115,8	-9,256	-7,956
DCASD 149.2	115,8	-9,472	-8,754
DCASD 154.1	116,8	-12,088	-9,187
DCASD 155.1	117	-9,671	-9,448

Spar Measurements

DCASC 64.5	76,8	-11,797	-17,4
DCASC 65.5	77	-11,559	-16,9
DCASC 86.5	81,2	-18,393	-14,1
DCASC 94.5	82,8	-11,693	-15,210
DCASC 90.6	82	-11,887	-15,831
DCASC 90.5	82	-12,132	-16,234
DCASD 145.5	115	-10,350	-15,186
DCASC 30.5	70	-11,552	-15,844
DCASB 102.5	52,6	-11,339	-14,177